Maastricht University

Oral Mucosal Organoids as a Potential Platform for Personalized Cancer Therapy

Citation for published version (APA):

Document status and date:
Published: 01/07/2019

DOI:
10.1158/2159-8290.CD-18-1522

Document Version:
Publisher's PDF, also known as Version of record

Document license:
Taverne

Please check the document version of this publication:

• A submitted manuscript is the version of the article upon submission and before peer-review. There can be important differences between the submitted version and the official published version of record. People interested in the research are advised to contact the author for the final version of the publication, or visit the DOI to the publisher's website.
• The final author version and the galley proof are versions of the publication after peer review.
• The final published version features the final layout of the paper including the volume, issue and page numbers.

Link to publication

Download date: 31 May. 2024

RESEARCH ARTICLE

Oral Mucosal Organoids as a Potential Platform for Personalized Cancer Therapy

Else Driehuis[1], Sigrid Kolders[1], Sacha Spelier[1], Kadi Lõhmussaar[1], Stefan M. Willems[2], Lot A. Devriese[3], Remco de Bree[4], Emma J. de Ruiter[2], Jeroen Korving[1], Harry Begthel[1], Johan H. van Es[1], Veerle Geurts[1], Gui-Wei He[1], Richard H. van Jaarsveld[1], Rurika Oka[5], Mauro J. Muraro[1,6], Judith Vivié[1,6], Maurice M.J.M. Zandvliet[7], Antoni P.A. Hendrickx[8], Nino Iakobachvili[9], Priya Sridevi[10], Onno Kranenburg[11], Ruben van Boxtel[5], Geert J.P.L. Kops[1], David A. Tuveson[10], Peter J. Peters[9], Alexander van Oudenaarden[1], and Hans Clevers[1,5]

ABSTRACT Previous studies have described that tumor organoids can capture the diversity of defined human carcinoma types. Here, we describe conditions for long-term culture of human mucosal organoids. Using this protocol, a panel of 31 head and neck squamous cell carcinoma (HNSCC)–derived organoid lines was established. This panel recapitulates genetic and molecular characteristics previously described for HNSCC. Organoids retain their tumorigenic potential upon xenotransplantation. We observe differential responses to a panel of drugs including cisplatin, carboplatin, cetuximab, and radiotherapy *in vitro*. Additionally, drug screens reveal selective sensitivity to targeted drugs that are not normally used in the treatment of patients with HNSCC. These observations may inspire a personalized approach to the management of HNSCC and expand the repertoire of HNSCC drugs.

SIGNIFICANCE: This work describes the culture of organoids derived from HNSCC and corresponding normal epithelium. These tumoroids recapitulate the disease genetically, histologically, and function-ally. *In vitro* drug screening of tumoroids reveals responses to therapies both currently used in the treatment of HNSCC and those not (yet) used in clinical practice.

See related commentary by Hill and D'Andrea, p. 828.

INTRODUCTION

The oral cavity, pharynx, and larynx are lined by a strati-fied mucosa that protects the underlying structures. These epithelia are keratinizing or nonkeratinizing, depending on the anatomic location (1). Neoplasias commonly arise in this epithelium, with a worldwide incidence of more than half a million patients a year (2). Well-known risk factors are alcohol and tobacco (3). Treatment of head and neck squamous cell carcinomas (HNSCC) is difficult, partly because of their anatomic location that complicates surgery, and partly due to the highly variable treatment response. Advanced cases require combinations of sur-gery, radiotherapy, and chemotherapy. Taken together, this results in relapse rates of more than 50% (4). Currently, there are no reliable models to predict therapy outcome and guide treatment decisions.

In vitro studies of this epithelium have relied on tumor-derived two-dimensional (2-D) cell lines (5) and on pri-mary keratinocyte cultures (6). Success rates to establish

[1]Oncode Institute, Hubrecht Institute, Royal Netherlands Academy of Arts and Sciences (KNAW) and University Medical Center Utrecht, Utrecht, the Netherlands. [2]Department of Pathology, University Medical Center Utrecht, Utrecht, the Netherlands. [3]Department of Medical Oncology, University Medical Center Utrecht, Utrecht, the Netherlands. [4]Depart-ment of Head and Neck Surgical Oncology, University Medical Center Utrecht, Utrecht, the Netherlands. [5]Princess Maxima Center, Utrecht, the Netherlands. [6]Single Cell Discoveries, Utrecht, the Netherlands. [7]Depart-ment of Clinical Sciences of Companion Animals, Faculty of Veterinary Medicine, Utrecht University, the Netherlands. [8]Department of Medical Microbiology, University Medical Center Utrecht, Utrecht, the Nether-lands. [9]M4I Division of Nanoscopy, Maastricht University, Maastricht, the Netherlands. [10]Cold Spring Harbor Laboratory, Cold Spring Harbor, New York. [11]Utrecht Platform for Organoid Technology (U-PORT), Utrecht Medical Center Utrecht, Utrecht, the Netherlands.
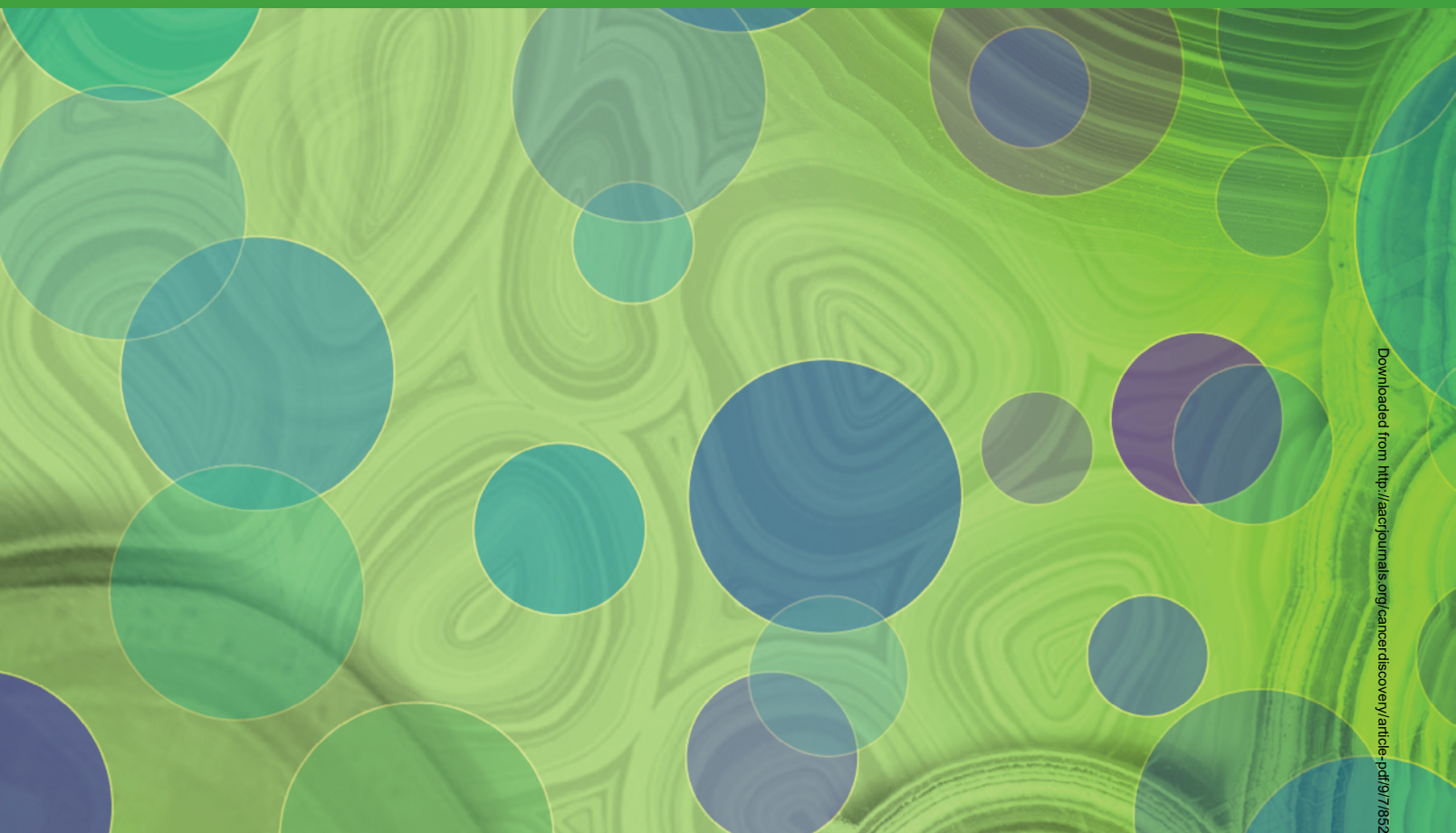
HNSCC-derived cell lines range from 11% to 33% (7). For primary keratinocyte cultures, keratinocytes are grown on feeder cells (mouse fibroblasts) in 2-D and have a limited lifespan. *In vitro* drug screens of 2-D lines have been used to characterize variability in drug response among tumors and as a tool to understand resistance mechanisms of tumor cells (8, 9). In an attempt to overcome limitations of these 2-D systems (10, 11), HNSCC lines have been replated in a three-dimensional (3-D) format. Compared with 2-D cell lines, these 3-D models better recapitulate characteristics of *in vivo* HNSCC (12, 13). In addition to *in vitro* models, HNSCC xenograft mouse models were introduced more than 30 years ago (14). Moreover, transgenic mouse models have been developed to understand molecular drivers of HNSCC tumorigenesis (15). Although these models provided important insights into HNSCC, they are lacking the potential for a personalized approach. Recently, two studies have reported on the generation of 3-D HNSCC cultures, giving an initial description of this technology (16, 17).

The oral mucosa can be subject to viral infection (18). Herpes simplex virus (HSV) is among the most commonly encountered viral infections of the oral cavity (18). HSV is known to infect keratinocytes and give rise to herpes labialis (cold sores; ref. 19). Infection with human papillomavirus (HPV) is associated with oropharyngeal HNSCC and characterizes a genetically distinct subgroup of tumors with better prognosis than HPV⁻ HNSCC (20). *In vitro* culture systems to study the interaction of keratinocytes with HPV are limited to the use of immortalized cell lines, or to primary cells that can only be cultured short-term (21).

Protocols to grow organoids from adult human tissues have been described for single-layered (simple) or (pseudo)stratified epithelia, such as those that line the colon, intestine, liver, pancreas, stomach, esophagus, prostate, lung, breast, and fallopian tube, and cancers derived thereof (22). Tumor organoids have previously been shown to phenocopy the tumor from which they are derived, allowing *in vitro* drug responses to be linked to genetic alterations present in the original tumor (22). A recent study on gastrointestinal cancers documented a strong correlation between patient clinical outcome and the response of the corresponding tumor organoids (23).

Here, we set out to establish organoids from the epithelial lining of the oral cavity, larynx, and pharynx. Next, we apply these conditions to derive tumor organoids from patients with HNSCC and to explore their potential to aid personalized therapy.

RESULTS

Organoids Derived from Healthy Oral Mucosa Recapitulate Morphologic and Functional Characteristics and Can Be Used to Model Oral Mucosa Pathology

To propagate organoid formation, we tested a range of media compositions described in previously published protocols for growth support of oral mucosa. Conditions that

American Association for Cancer Research

were successful to grow mouse tongue epithelium (see Supplementary Fig. S1A and S1B) were refined on human material obtained from surgical resections. In brief, the epithelial layer was microdissected from the surgical specimen to remove fat and muscle, digested in 0.125% trypsin, and filtered, and the resulting cell suspension was then plated in Basement Membrane Extract (BME), a Matrigel equivalent (Fig. 1A). Within the first few days after plating, organoids grew out from single cells or small cell clumps (Supplementary Fig. S2A; Supplementary Movie S1). Over time, these organoids developed into dense structures, often with keratinized centers (Fig. 1B). On average, organoids could be passaged within 10–14 days. After the first passages, organoids typically expanded exponentially, being passaged every 10 days with a split ratio of 1:5 (Supplementary Movie S2). We received surgical material from 40 patients, of which 26 (65%) grew out into organoids. Established organoid lines could be expanded long-term (> 15 passages) and could be cryopreserved and recovered successfully. We assessed proliferative potential over 5 passages in expansion medium (Fig. 1C) and observed unabated exponential growth. Scanning electron microscopy revealed that organoids are composed of tightly connected cells (Supplementary Fig. S2B). Immunohistochemical (IHC) staining for basal cell marker *TP63* and proliferation marker *MKI67* of paraffin-embedded organoids showed that the organoids recapitulate the tissue of origin. Proliferative $MKI67^+/TP63^+$ basal cells were located in the external organoid layer touching the basal membrane substitute BME, recapitulating the tissue of origin (Fig. 1D). Differentiation marker KRT13 was detected in cells in the interior of the organoid. Characteristics of keratinocytes such as abundant tonofilaments and desmosomes were observed using transmission electron microscopy (Supplementary Fig. S2C). Upon withdrawal of growth factors from the medium, differentiation increased, as shown by a >45-fold increase in KRT13 expression, and halted proliferation (decreased expression of *MKI67*; Fig. 1E; Supplementary Fig. S2D). Finally, we assessed the genetic stability of normal tongue epithelium–derived organoid by metaphase spread analysis and observed normal numbers of chromosomes at passage 6 (median 46 ± 0.42, $n = 26$) and at passage 16 (median 45 ± 0.34, $n = 33$; Fig. 1F).

Oral Mucosa Organoids Can Be Productively Infected with HSV and HPV

We explored the use of this model to study viral infection with HSV type 1 (HSV1), a virus known to infect keratinocytes (19) and to give rise to herpes labialis (cold sores). Using fluorescence microscopy, we followed infection of organoids with tdTomato-labeled HSV (ref. 24; Supplementary Fig. S3A). Using live imaging, spreading of the infection in organoids was observed two days after initial infection (Fig. 1G; Supplementary Movie S3). After two weeks in culture, infection had spread throughout entire organoids (Fig. 1H). Infection of organoids resulted in an increase in viral DNA, which could be inhibited by the addition of acyclovir (viral tyrosine kinase inhibitor) in all three organoid lines tested (Supplementary Fig. S3B).

As HPV is known to contribute to oncogenesis of a subset of HNSCC tumors (3, 25), HPV16 particles were used to infect oral mucosa organoids (26). Viral replication was quantified by increase in HPV DNA levels (Supplementary Fig. S3C). After splitting of the organoids, an increase in HPV DNA could

be observed, implying lasting infection (Supplementary Fig. S3D). Finally, transfer of filtered supernatant taken 12 days postinfection from infected organoids resulted in reinfection, proving virion production in organoids (Supplementary Fig. S3E). Taken together, we conclude that oral mucosa–derived organoids allow infection with HSV1 and HPV16, validating the organoid model as an *in vitro* model for mucosal pathology.

HNSCC Tumoroids Recapitulate Molecular and Morphologic Characteristics of the Original Tumor

We next set out to grow organoids from patient-derived HNSCC samples, obtained from either surgical resections or biopsies. We successfully established tumoroids from 31 patients, ranging in age from 48 to 91 (average age at diagnosis: 69). Tumoroids were established from tumors originating in the oral cavity (floor of mouth, tongue, and gingiva/alveolar process), pharynx, larynx, salivary gland, nasal cavity, and neck (Fig. 2A). Patient clinical data corresponding to established organoid lines can be found in Supplementary Table S1. Of the 31 established tumoroid lines, 16 were fully characterized molecularly at the date of first submission (data on all others will be added when these become available). These lines were named T1, T2, T3, etc., whereas the corresponding normal epithelium–derived lines were termed N1, N2, N3, etc. The success rate to establish organoids from tumor tissue was approximately 60%. Tumoroids grew either as dense structures (similar to the normal wild-type epithelial organoids) or as cystic structures (Supplementary Figs. S4 and S5). Tumoroids derived from different patients showed different morphologies, as based on brightfield microscopy (Supplementary Fig. S4) and hematoxylin and eosin (H&E) staining (Supplementary Fig. S5). Comparison of organoids with the original tumor tissue and adjacent normal epithelium of the same patient revealed tumor-specific histopathologic changes that were retained in culture (Supplementary Fig. S6).

Comparing IHC stainings of the primary tumor specimens with the corresponding tumoroids revealed that these retained histologic characteristics of the epithelial tumor cells (Fig. 2B). However, as described for other adult tissue–derived organoids, tumoroids contain only the transformed epithelial tumor cells, not the immune, connective tissue, or vessel elements. This was evident by the keratin staining that marks all cells of the organoids, but only the epithelial component of the tumor section (Fig. 2B).

A complication of growing tumoroids from other carcinoma types has been the gradual overgrowth by normal wild-type organoids (27, 28). To confirm the tumor identity of our tumoroids, several approaches were taken. Nutlin-3, an MDM2 agonist, prevents the growth of p53 wild-type cells (29). We observed that 10 of the 14 lines tested (71%) grew in the presence of Nutlin-3 (Supplementary Fig. S7), in agreement with the approximately 75% of HNSCC carrying inactivating *TP53* mutations (30). For example, N1 organoids (*TP53* wild-type) died in the presence of Nutlin-3, whereas tumoroid line T1 did not (Fig. 2C). *TP53* staining on fixed organoid sections confirmed the *TP53* status (Fig. 2D): *TP53* staining is caused by accumulation of mutant protein, a clinical parameter to determine the presence of mutant *TP53* protein (31).

We performed transcriptome analysis of nine normal organoid lines and seven tumoroid lines. As a quality control, two
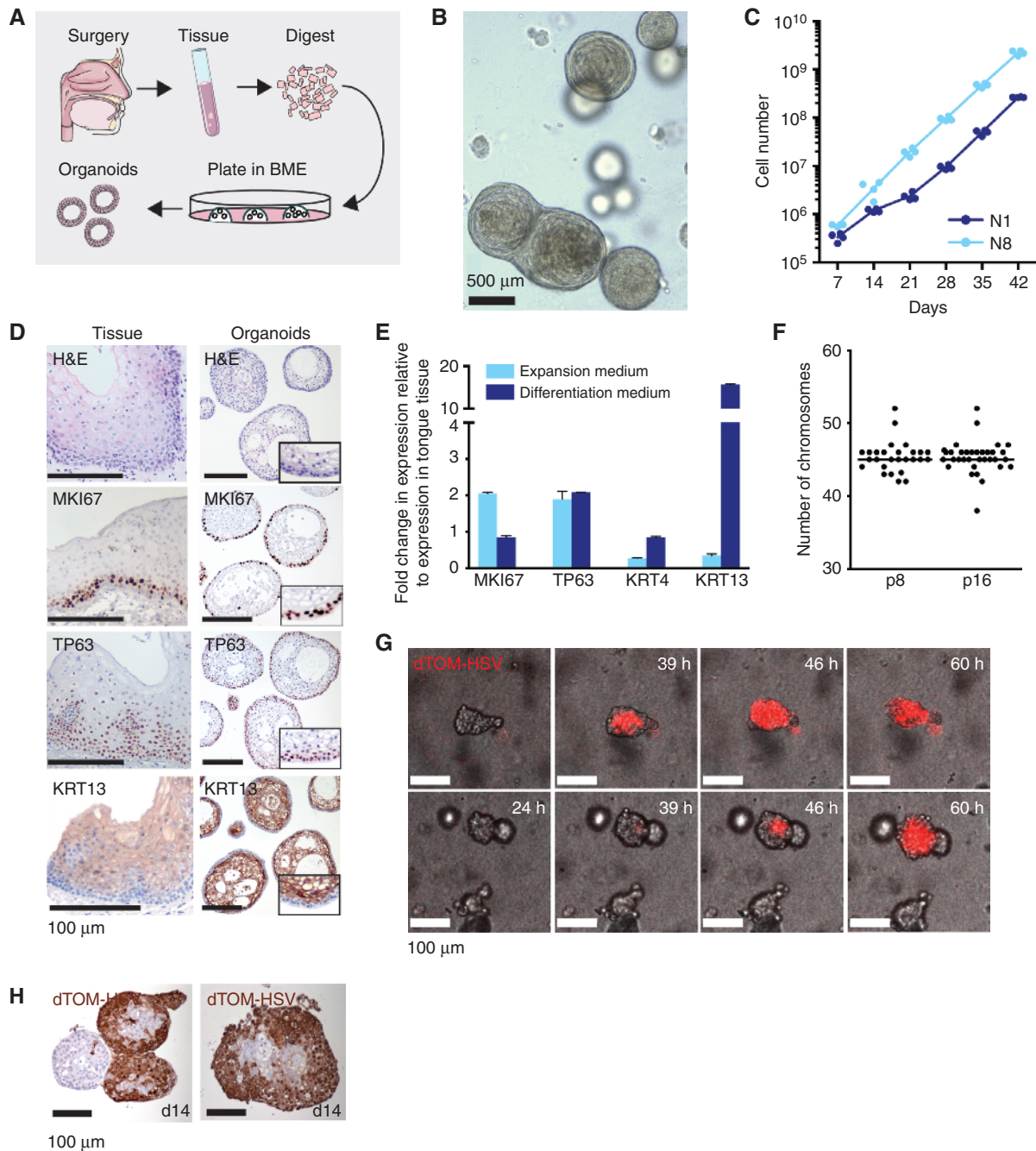
Figure 1. Organoids can be derived from healthy oral mucosa, recapitulate morphologic and functional characteristics, and can be used to study oral mucosa pathology. **A,** Schematic outline of the digestion and initial culture condition of oral mucosa organoids. If the patient supplies informed consent, tissue that is obtained via biopsy or resection is collected, digested using trypsin, and subsequently plated. Over time, organoids grow out from the primary tissue. Images obtained from https://smart.servier.com/. **B,** Brightfield microscopy image of an organoid line derived from oral mucosa epithelium. Scale bar, 500 μm. **C,** Total cell numbers obtained from organoid cultures over the course of 6 weeks. Cell numbers were determined in two independently established normal oral mucosa organoid lines (N1 and N8). Counting was performed in quadruplicate. Quantification shows stable growth of the organoid lines. **D,** Hematoxylin and eosin (H&E) staining and immunostaining for MKI67, TP63, and oral mucosa–specific KRT13 of paraffin-embedded N8 organoids and control tissue. As can be seen, proliferating basal cells (*MKI67* and *TP63*–positive) reside in the periphery of the organoids, whereas more differentiated keratinocytes (KRT13-positive) reside in the center of the organoid. Scale bars, 100 μm. **E,** Quantitative PCR of a normal oral mucosa organoid line (N5) for proliferation marker *MKI67*, basal cell marker *TP63*, and *KRT13*. Prior to RNA collection, growth factors were withdrawn from the medium to induce differentiation. Expression levels are calculated using $\Delta\Delta C_t$ method. For each marker, fold change in expression is shown relative to expression of this marker in human primary tongue tissue, which is set to 1. $n = 3$, individual data points are shown, bars represent average. **F,** Number of chromosomes was determined for N8 organoids in early passage (p8) and later passage (p16) by metaphase spread analysis. **G,** Live cell imaging of dTOM-HSV infected organoids. Two organoids were followed over time and pictures of the following timepoints are depicted in this figure: $t = 0$, 24, 39, 46, and 60 hours. Scale bars, 100 μm. **H,** IHC staining for dTomato performed on paraffin-embedded organoids that were infected with HSV-dTomato and maintained in culture for two weeks, Scale bars, 100 μm.
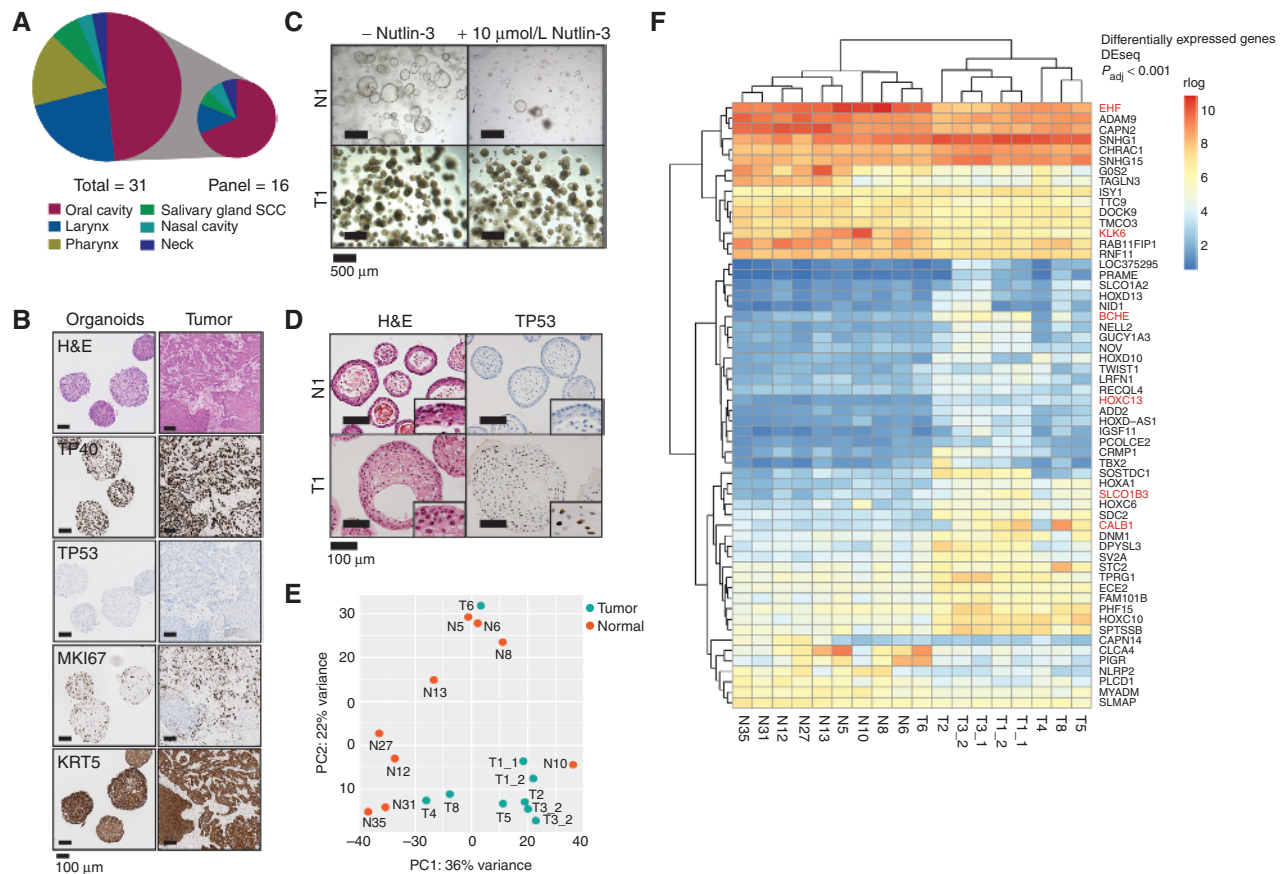
Figure 2. HNSCC organoids can be established and recapitulate functional and morphologic characteristics of the tumor. **A,** Overview of the tumors of which organoids were established in this study and their anatomic location. SCC, squamous cell carcinoma. **B,** Hematoxylin and eosin (H&E) staining and immunostaining for basal cell marker TP40, tumor suppressor TP53, proliferation marker MKI67 and KRT5 of paraffin-embedded T15 organoids and corresponding tissue. Scale bars, 100 μm. **C,** Organoids established from HNSCC and corresponding normal tissue of the same patient show a different response to MDM2 agonist Nutlin-3. Scale bars, 500 μm. **D,** H&E and immunostaining for TP53 performed on sections of paraffin-embedded organoids reveal differences in morphology and *TP53* status of the two organoid lines. Scale bars, 100 μm. **E,** Principal component analysis of RNA-sequencing data of 9 normal wild-type (orange) and 7 tumor organoid lines (blue). Two tumor samples were sequenced in two independent runs as a quality control. These samples cluster together. Tumor-derived organoid cluster together and away from the normal wild-type epithelium–derived organoids. There are two exceptions to this clustering, as N10 and T6 do not cluster together with the other normal and tumor-derived organoid lines, respectively. **F,** Heat map depicting expression of the 58 differentially expressed genes between normal and tumor-derived organoids ($P_{adj} < 0.001$) in the sequenced organoids. Blue indicates low expression, red indicates high expression. Differential expression was calculated as described in DESeq2 package (32). Genes marked in red are described in the text and were reported by others to be differentially expressed in HNSCC. For these genes, Supplementary Fig. S8 shows the expression values relative to normal organoids.

tumor organoid lines (T1 and T3) were sequenced twice in two independent runs. Samples from independent runs clustered together. To determine the contribution of the cancerous state to the total variability in gene expression, principal component analysis (PCA) was performed. PCA revealed segregation of normal and tumor organoids into different clusters, with the exception of tumoroid line T6 (with confirmed mutations in *TP53* and *CDKN2A*) clustering within the normal wild-type organoid group, and normal line N10 not clustering with the other normal samples (Fig. 2E). In addition, we used DESEQ2 analysis to explore the potential to identify or validate tumor biomarkers using HNSCC organoids (32). A search for differentially expressed genes between normal and tumor samples resulted in detection of 857 genes ($P_{adj} < 0.0001$). Among the 58 most differentially expressed genes ($P < 0.01$) we found genes of which the expression has been described to be altered in HNSCC, including *KLK6, SLCO1B3,*

HOXC13, CALB1, EHF, and *BCHE* (refs. 33–38; Fig. 2F; Supplementary Fig. S8; Supplementary Table S2).

Tumoroids Recapitulate Genetic Alterations Found in HNSCC

Targeted sequencing (on a panel of 54 oncogenes or tumor suppressors relevant to HNSCC, in one case an extended oncopanel of 140 genes; n = 14; Fig. 3A) or whole-exome sequencing (n = 2; Fig. 3B) was performed on a subset of the HNSCC organoid lines (Supplementary Tables S3 and S4).The most commonly mutated gene, *TP53*, was genetically altered in 11 of the 16 tumor lines (69%). As expected, no *TP53* mutations were detected in the Nutlin-3–sensitive lines T8, T9, T10, T20, and T27. *PIK3CA* was altered in 7 of the 16 tumoroid lines. *KRAS* was mutated in four cases, although often mutations were detected at low frequency. *BRAF, CDKN2A, FAT1,* and *PDGFRA* were mutated in two cases. Genes affected in one
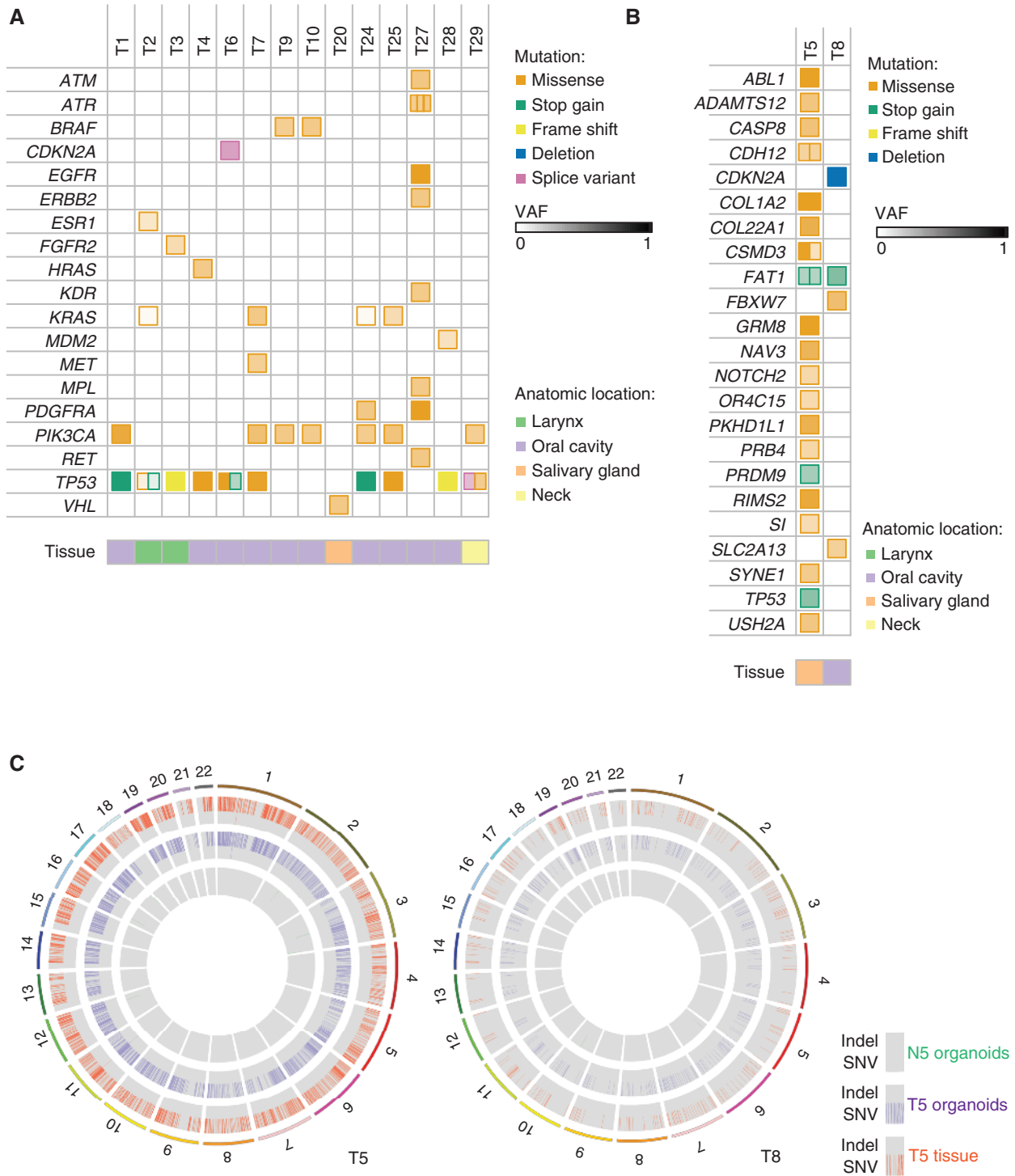
Figure 3. HNSCC-derived organoids recapitulate genetic alterations found in this tumor type. **A** and **B,** Mutations detected in HNSCC-derived organoids that were sequenced using targeted sequencing (**A**) or whole-exome sequencing (**B**). The color of the square indicates the type of mutation detected: missense (orange), stop/gain (green), frameshift (yellow), deletion (blue), splice acceptor (purple). Color intensities indicate the variant allele frequency (VAF) of the detected genetic alteration. Anatomic source of the organoid line is shown: oral cavity (purple), larynx (green), or parotis (orange). **C,** Circos plots of T5 and T8, showing the single nucleotide variants (SNV; outer track) and small insertions or deletions (Indel; inner track) for tumor tissue (orange), tumor organoids (purple), and wild-type organoids (green). All variants are shown relative to wild-type tissue.

American Association for Cancer Research

case include *ABL, ATR, ESR1, FGFR2, HRAS, MDM2, MET*, and *VHL*. In three cases (T3, T5, and T8), we sequenced both the original tumor and the tumoroid line (see Supplementary Fig. S9) and observed an enrichment of the variant allele frequency (VAF) of the detected mutations. Most likely, this is due to the purely epithelial character of tumoroids, whereas the primary tumor sample also contains immune cells and vasculature and stromal components in addition to the tumor epithelial cells. As T5 and T8 were subjected to whole-exome sequencing, mutations were also detected in genes that were not included in the targeted sequencing panel. Those mutation lists were filtered for those present in genes most commonly affected in HNSCC (39). Using this criterion, we detected pathogenic mutations in 20 (T5) and 4 (T8) HNSCC cancer-associated genes (Fig. 3B). For both tumor organoids, corresponding normal organoids were also sequenced, to confirm the absence of any of the mutations detected in the tumor lines. Subsequently, we scrutinized all single-nucleotide variants (SNV) and small insertions or deletions (Indel) throughout the genome in the tumor and normal tissue as well as in N5 and T5 organoids (Fig. 3C). For both samples, both the tumor tissue and the tumoroids showed SNVs and Indels that were absent from the normal tissue. Moreover, tumoroids largely recapitulated the genetic alterations that were detected in the tumor. Normal organoids and normal tissue lacked these genetic alterations, confirming that these organoids consisted of normal (nontumor) cells.

HNSCC-Derived Organoids Are Chromosomally Unstable *In Vitro*

Chromosome missegregation underlies the aneuploidies frequently observed in human tumors (40). Increased missegregation rates result in the phenotype known as chromosomal instability (CIN), which is commonly observed in cancers, including HNSCC (41). To investigate whether CIN was also present in HNSCC tumoroids, we assessed chromosome segregation in a matched normal and tumor organoid line. Organoids labeled with Histone2B-mNeon were imaged using a spinning-disc confocal microscope to visualize the chromatin during cell division (42). T1 showed elevated levels of chromosome segregation errors when compared with its normal counterpart, N1 (Fig. 4A; Supplementary Movies S4 and S5). The majority of cells in N1 showed no signs of chromosome missegregation (Fig. 4B), whereas T1 showed a variety of segregation errors, including anaphase bridges and binucleated cells undergoing multipolar division (Fig. 4C and D, respectively). We conclude that T1 has acquired CIN during oncogenic transformation. CIN can result in aneuploidy, by the loss or gain of (parts of) chromosomes (40). In agreement, quantification of the number of chromosomes in cells of N1 and T1 using metaphase spreads revealed that this number was much more variable in T1 than it was in N1 (Fig. 4E). Other tumoroid lines also carried aberrant chromosome numbers, with T3 and T4 being tetraploid (Fig. 4F), whereas organoids derived from corresponding normal tissue contained normal numbers of chromosomes.

HNSCC Tumoroids Recapitulate Characteristics of HNSCCs upon Xenotransplantation

To assess whether tumorigenic potential of the cultured HNSCC cells was retained, we subcutaneously transplanted tumoroids into mice. Injection of the normal organoids did not result in outgrowth, whereas transplantation in all three tumor lines yielded macroscopically visible tumors after 6 weeks in at least 2 of 3 mice ($n = 3$ for each organoid line; Fig. 5A). For all tumors, H&E staining revealed stratification and keratinization characteristic of HNSCC (Fig. 5B; Supplementary Fig. S10). Staining for human nuclei showed positive, thus proving the origin of the tumors from the injected human-derived organoids. Comparison of proliferating cells, measured by *MKI67* staining, revealed differences in proliferation among the distinct organoid lines (Fig. 5C). These characteristics were retained between mice that were transplanted with the same organoid line (Supplementary Fig. S10). The tumor cells displayed levels of atypia that were regarded as cancerous (assessed by a pathologist). Tripolar mitotic figures and nuclear pleomorphism were observed (Fig. 5D). Moreover, muscle invasion was observed in one case (Fig. 5E). Taken together, this shows that HNSCC organoids retain tumorigenic potential in culture and can form HNSCC with features similar to the parental tumor, upon subcutaneous transplantation into mice.

HNSCC Tumoroids as a Platform for Drug Screening

The genetic alterations found in HNSCC are commonly found in other tumor types, and therapies targeting some of these specific mutations exist. Regardless, with the exception of cetuximab, an anti-EGFR antibody that is used in treatment of HNSCC, no targeted therapies are currently applied in standard care of these patients (43–46). In recent years, it has become clear that mutation status alone does not provide the required specificity or sensitivity to serve as a predictive marker (47). For this reason, we tested a panel of organoid lines carrying different genetic alterations that are regularly found in HNSCC for their *in vitro* drug sensitivity (Supplementary Fig. S11A).

To refine our *in vitro* drug screening assay, we used Nutlin-3 treatment. Exposure to a concentration series allowed quantitative discrimination between sensitive and nonsensitive lines (Fig. 6A). As expected, *TP53* wild-type cells were sensitive to Nutlin-3 exposure, whereas *TP53*-mutant organoids were not (Fig. 6B). The assay was reproducible ($n = 3$; Supplementary Fig. S11B). To assure quality of the drug screening data, a Z factor score (a measure of assay quality) was calculated for each drug screen in this study (Supplementary Fig. S11C). Average Z factor score was 0.7 (ranging from 0.3 to 0.92), which is consistent with an experimentally robust assay.

Subsequently, we exposed 13 fully characterized tumoroid lines (tumoroid lines T10 and T29 did not survive the robotized drug screening procedure) to cisplatin, carboplatin, and cetuximab, drugs currently used in the treatment of patients with HNSCC. Using *in vitro* concentrations similar to plasma concentrations reached in patients with HNSCC (48), we observed differential sensitivity of the organoids to these compounds. On the basis of the measured IC_{50}, we made a ranking of the tumoroid lines tested for cisplatin and carboplatin (Fig. 6C). Although IC_{50} values for cisplatin and carboplatin were different (average $IC_{50}^{cisplatin}$ was 5.91 µmol/L and $IC_{50}^{carboplatin}$ was 44.1 µmol/L), correlation between cisplatin and carboplatin sensitivity was observed (Pearson correlation, $r = 0.64$, $P < 0.05$; Fig. 6D; Supplementary Fig. S12). This correlation
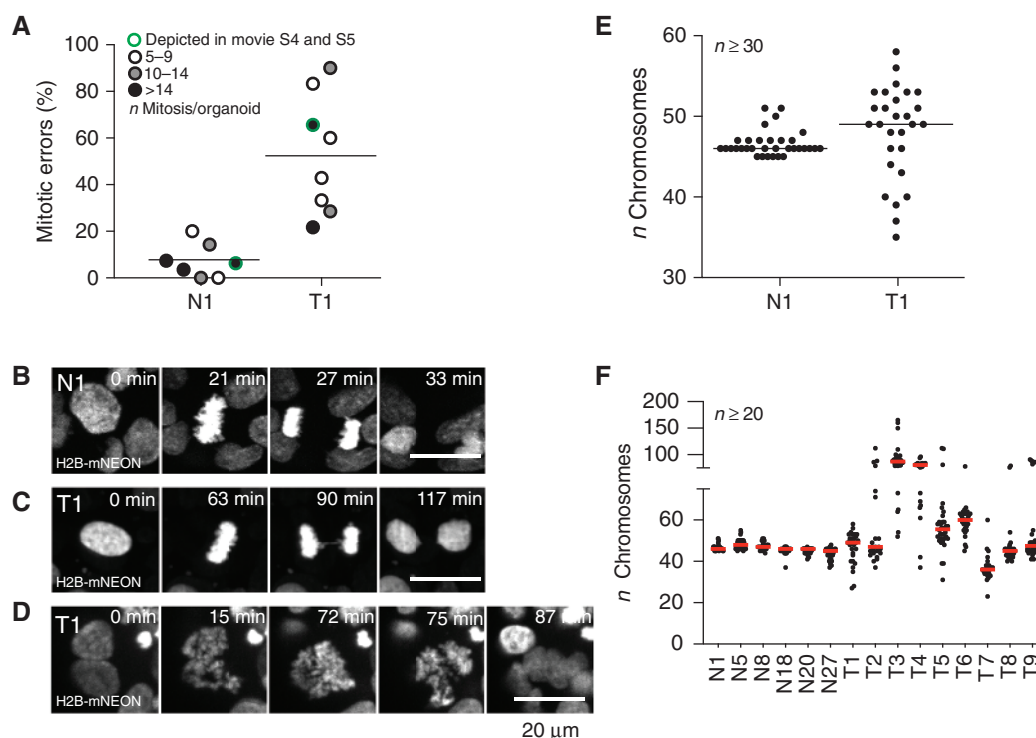
Figure 4. HNSCC-derived organoids are chromosomally unstable *in vitro*. Imaging of H2B-mNEON expressing organoids reveals cell divisions that can be studied and quantified for segregation errors during division. **A,** Quantification of segregation errors observed in N1 and T1. Percentage of mitotic errors per organoids is shown. One dot represents an imaged organoid, and the color of the dot indicates the corresponding number of mitoses. Green encircled dots represent the organoids that are shown in Supplementary Movie S4 and S5. **B–D,** Stills taken from time-lapse movies of N1 and T1 organoids. Maximum projections of selected Z-planes are shown. **B,** Examples of a correct mitosis observed in N1. **C,** Example of an anaphase bridge formed during mitosis in T1. **D,** Example of a binucleated cell undergoing multipolar division observed in T1. Scale bars, 20 μm. **E,** Scatter plot presenting chromosome number distribution and median, based on organoid metaphase spreads of N1 and T1 cells. **F,** Scatter plot depicting chromosome number distribution and median.

has previously been described in ovarian cancer cells (49). *In vitro* platinum–DNA adduct formation has shown that both drugs give rise to the same damage, yet cisplatin does so at lower dose (50). Although the mechanism of action is the same, it is suggested that cisplatin should be preferred over carboplatin as a radiosensitizer in HNSCC (51). We confirm that, for the lines tested here, none showed a higher sensitivity to carboplatin than to cisplatin.

Organoids were also exposed to the anti-EGFR antibody cetuximab, and differential responses were observed between different patient-derived organoid lines (Fig. 6E; Supplementary Fig. S12). Recent studies challenge the prognostic value of EGFR overexpression or increased gene copy number for cetuximab response (47). Here, no correlation between EGFR expression and cetuximab response was observed. Finally, we found that organoid lines insensitive to cetuximab commonly carried mutations downstream of *EGFR* (*PIK3CA, KRAS, HRAS*, or *BRAF*). This has important implications for patient inclusion for cetuximab therapy, which currently does not include genetic testing. Of note, RAS/RAF genetic testing is routinely performed in patients with colorectal cancer who are eligible for EGFR-targeting treatments.

Currently, treatment with curative intent for patients with advanced HNSCC consists of surgery with adjuvant radiotherapy, with or without chemotherapy, or radiotherapy with or without chemotherapy with the possibility of surgery as

salvage treatment in case of residual/recurrent disease (47). Radiotherapy can also be a part of palliative treatment to reduce pain or tumor invasion. Therefore, we tested the sensitivity of the tumoroids to ionizing radiation. We consistently observed differential responses between the tumoroid lines when exposed to radiotherapy. This suggested that clinical correlations could be studied (Fig. 6F). To assess whether expression profiles could predict responses to these therapies, we performed DEseq analysis, comparing organoid lines with different responses to either cisplatin and carboplatin, cetuximab, or radiotherapy (see Supplementary Fig. S13; Supplementary Table S5). Although differentially expressed genes could be detected in all comparisons, including those previously described associated with resistance to these therapies (52–55), no clear indication for resistance mechanisms could be deduced from performing gene enrichment analysis on these gene sets.

Correlation of *In Vitro* Organoid Responses with Clinical Responses in 7 Patients Who Received Radiotherapy

Seven of the patients received (postoperative) radiotherapy, which allowed a correlation with organoid sensitivity to this treatment. Although the number of patients is small, and these HNSCC tumors comprise a heterogeneous group (by anatomic location, timing (primary or adjuvant), and total
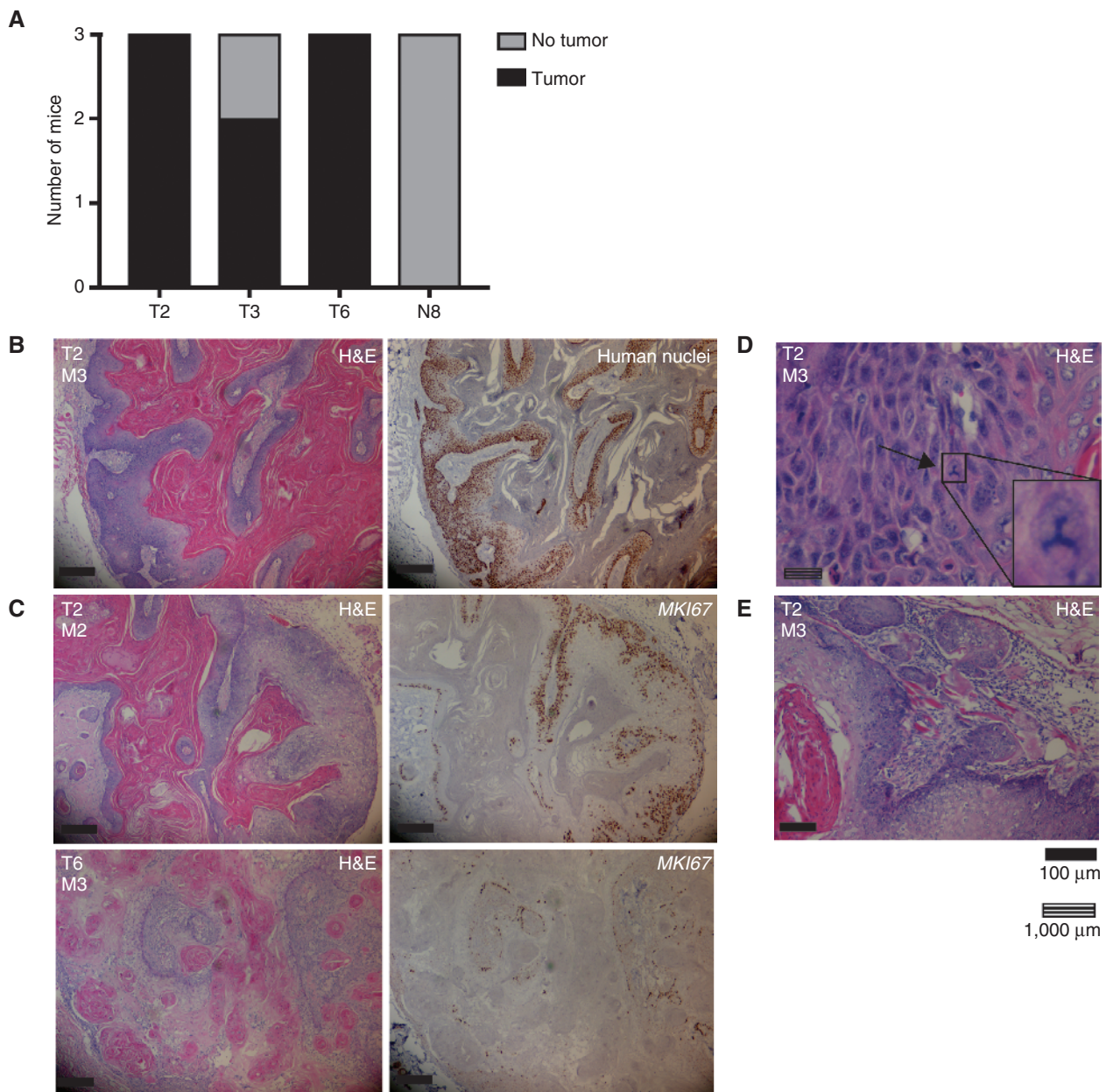
Figure 5. Xenografted HNSCC organoids recapitulate histopathologic characteristics of HNSCCs. **A,** Three independent mice were injected with each organoid line, and the number of mice that developed tumors is depicted. **B,** Hematoxylin and eosin (H&E) and antihuman nuclei staining of the paraffin-embedded tumor. Left, H&E reveals stratification from more basal (dark purple) to more differentiated keratinocytes (light purple) to eventually deposited keratin (pink). Right, immunostaining for human nuclei reveals human origin of the squamous epithelial cells observed in the tumor. **C,** Comparison of two tumors originating from either organoid line T2 or T6. Left, H&E reveals different morphology of the different tumors. Right panels, *MKI67* staining shows difference in the number of cells in G_1 between the two tumors. **D,** Example of atypia that can be observed in the tumors. Arrow indicates a tripolar mitotic figure. Throughout the image, nuclear pleomorphism can be observed. **E,** Squamous cells can invade into the surrounding muscle tissue of the mouse. Striped scale bar, 1,000 μm; black scale bars, 100 μm.

dose of irradiation given), we used this set to explore the potential of HNSCC organoids as a predictor for treatment response in the future. All patients described here were given radiotherapy with curative intent. An overview of the treatment details is given in Supplementary Table S6. Three of 7 patients relapsed after undergoing radiotherapy. Indeed, the three corresponding organoid lines were among the most resistant when exposed to radiotherapy *in vitro* (Fig. 6G).

Organoid line T3 showed the highest sensitivity to radiotherapy. Indeed, this patient had a lasting response to palliative radiotherapy. The primary tumor of the larynx received 48 Gy in 4 weeks and showed no signs of growth upon physical examination up to 5 months later, corresponding with ongoing local control due to radiotherapy. The patient unfortunately succumbed to lung carcinoma 5 months later. The patient from whom T5 was derived was treated with adjuvant

radiotherapy following surgery (stage T4aN0 parotid tumor) because of two prognostic factors that predict high risk of relapse of disease: macroscopic residual disease and perineural growth, observed in the resected tissue. The patient received a dose of 66 Gy over a period of 6 weeks at the parotid area. Nine months after completion of radiotherapy, the patient showed no signs of relapse or progression upon physical examination, showing a clinically good response to radiotherapy. Organoid lines T1 and T2 were not responsive to radiotherapy in the *in vitro* assay. Indeed, the patients corresponding to these lines showed progressive disease shortly after completing the treatment. Patient T1 presented with tongue squamous cell carcinoma (SCC; stage T2N2b) with extranodal growth and was treated with radiotherapy after resection of the primary tumor with positive margins. The patient received a dose of 66 Gy over the course of 10 weeks. Six months later, the patient complained of pain in the tumor area and locoregional relapse of disease was eventually diag-

nosed 3 months later, leading to death 3 months after that. Patient T2 presented with an SCC in the larynx (stage T2N0) for which 60 Gy of radiation was given. Four months later the patient presented with complaints. Five months later, a recurrent tumor was diagnosed that invaded the subglottis and required a complete laryngectomy. T25 was the organoid line most resistant to radiotherapy. These *in vitro* findings correlated well with the clinical history of patient T25. This patient presented with an SCC of the floor of mouth (stage T2N1). After receiving surgery for excision of the primary tumor and a selective neck dissection with negative margins, he developed a recurrence in the neck for which he was treated with radiotherapy. A total dose of 52 Gy was delivered to the neck. Only one month later, extensive regional recurrent disease (including skin metastases) in the neck was diagnosed upon physical examination. One month later, the patient succumbed to disease. Patient T27 was diagnosed with a floor of mouth SCC (stage T3N1) for which adjuvant radiotherapy
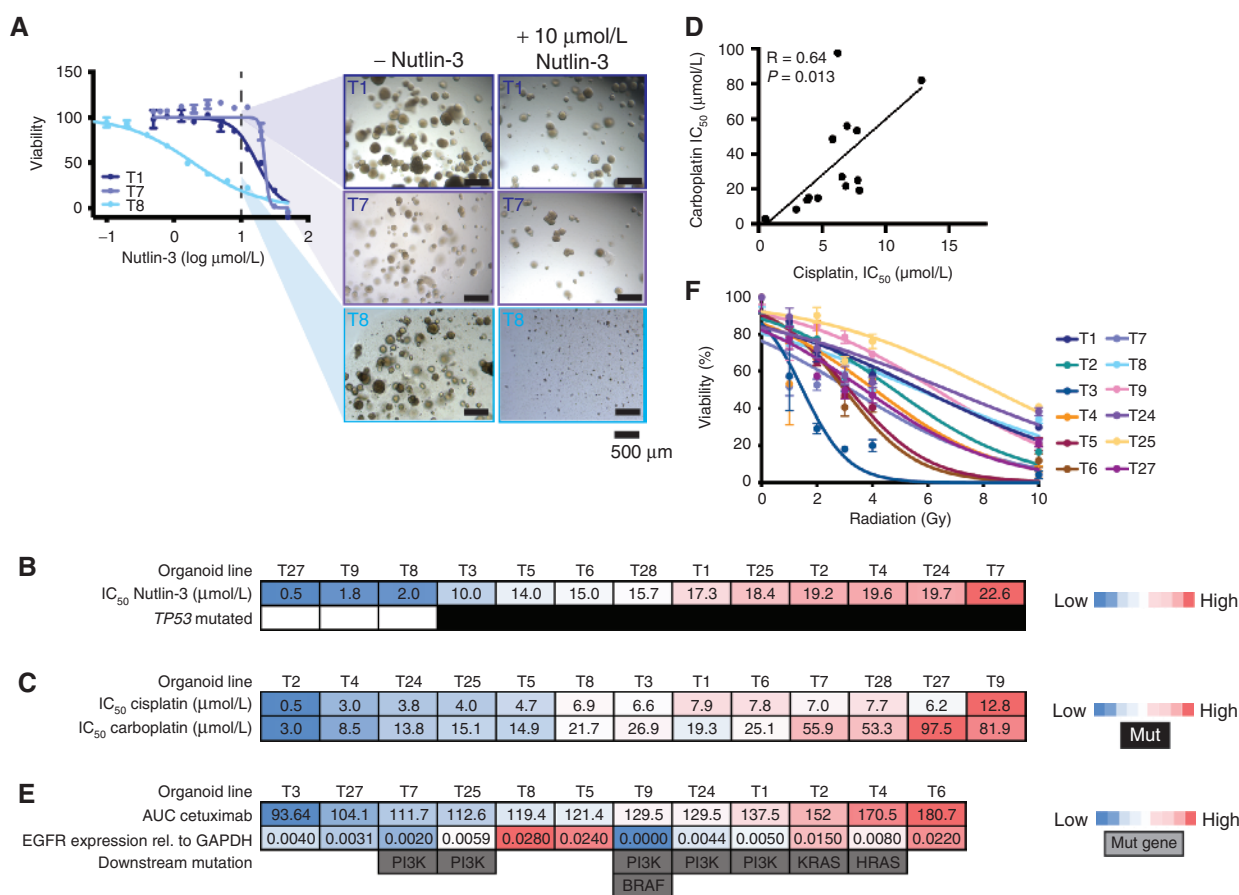

Figure 6. HNSCC organoids as a platform for drug screening. **A,** Validation of the drug screen set-up using Nutlin-3 exposure. Drug screen viability is consistent with the Nutlin-3 response observed using brightfield imaging. Scale bars, 500 μm. **B,** Heat map showing the tumoroids ranked on the basis of Nutlin-3 IC$_{50}$. Red indicates high IC$_{50}$ values, blue indicates low IC$_{50}$ values. IC$_{50}$ values and *TP53* mutation status are depicted. **C,** Heat map showing the organoid lines ranked on the basis of cisplatin and carboplatin sensitivity. Red indicates high IC$_{50}$ values, blue indicates low IC$_{50}$ values. **D,** Correlation between cisplatin sensitivity (*x*-axis) and carboplatin sensitivity (*y*-axis) can be observed *in vitro*. Pearson correlation, $r = 0.71$, $P < 0.05$. Each dot represents one tumoroid line, for which the cisplatin IC$_{50}$ value is plotted on the *x*-axis, and the carboplatin IC$_{50}$ value is plotted on the *y*-axis. **E,** Heat map showing the organoid lines ranked on the basis of cetuximab sensitivity as measured by AUC. Here, AUC was used instead of IC$_{50}$ values, because of the curvature of the kill curve that did not allow for IC$_{50}$ value calculation. Red indicates high AUC values, blue indicates low AUC values. In this dataset, no correlation between EGFR expression and cetuximab sensitivity can be observed. Mutations in downstream components of the EGFR pathway (PIK3CA, KRAS, HRAS, and BRAF) confer resistance to cetuximab. **F,** Organoids show variable sensitivity to radiation. Cell viability is plotted on the *y*-axis for different amounts of radiation, ranging from 0 to 10 Gy (*x*-axis). (*continued on next page*)
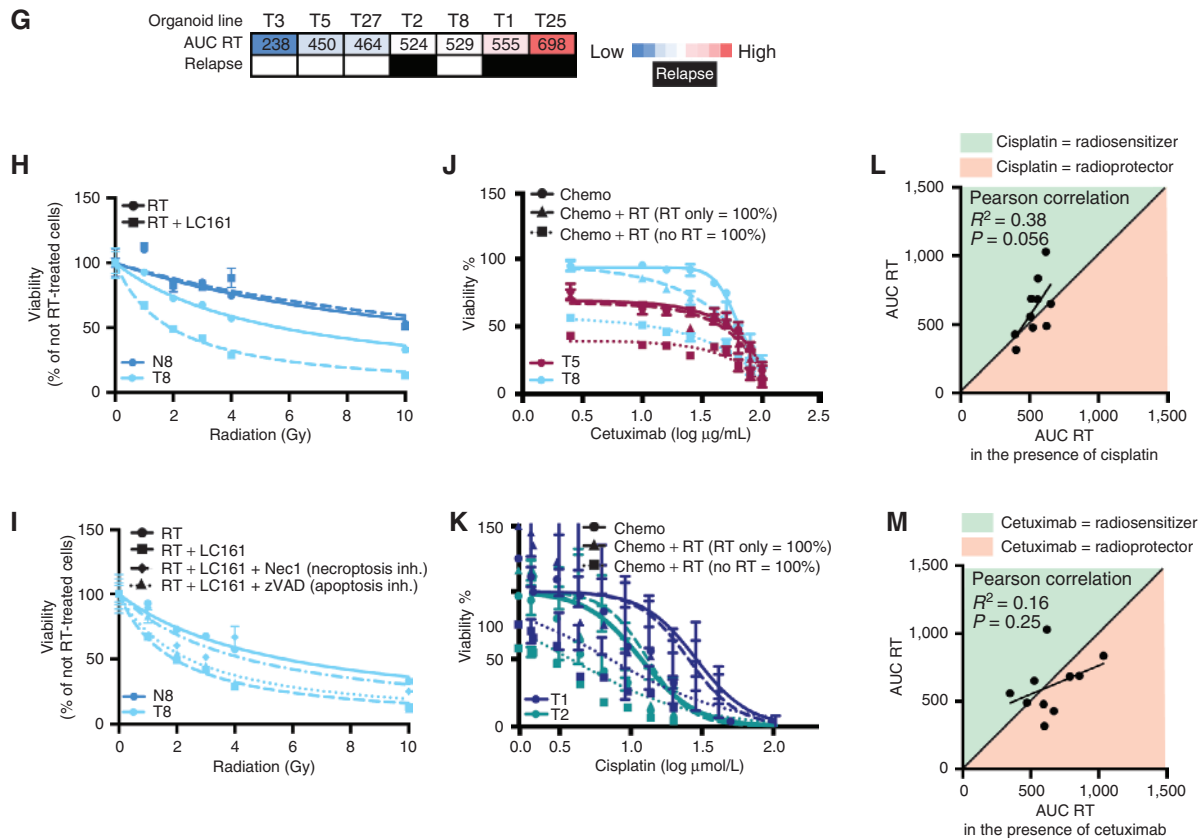
Figure 6. *(Continued)* **G,** Heat map showing the organoids ranked on the basis of radiotherapy sensitivity as measured by AUC. Red indicates high AUC values, blue indicates low AUC values. The row below summarizes the clinical response of patients, where a black box indicates a relapse after completion of radiotherapy treatment. **H,** Radiotherapy (RT) sensitivity of T8 and N8 organoids in the presence (dashed line, square symbols) or absence of 1 µmol/L LC161. For cells exposed to radiation in the presence of LC161, viability was calculated relative to organoids treated with LC161 alone. **I,** Exposure of T8 cells to radiotherapy alone, radiotherapy + LC161, and radiotherapy + LC161 in the presence of either necroptosis inhibitor (Nec1; diamonds) or apoptosis inhibitor (zVAD; triangles). For cells exposed to radiotherapy in the presence of any of the used compounds, viability was calculated relative to organoids treated with these compounds alone. **J** and **K,** Chemoradiation therapy of tumoroids. Cisplatin and cetuximab screens were performed either in the presence ["chemo + radiotherapy (no radiotherapy = 100%)"] or absence ("chemo") of radiation. Viability was calculated relative to untreated (no chemo, no radiotherapy) organoids, for which viability was set to 100%. To depict the effect of chemotherapy only, in the presence of radiotherapy, viability of the radiated tumoroids was calculated relative to tumoroids that were exposed to radiation, but no chemotherapy. This result is depicted by the line "chemo + radiotherapy (radiotherapy only = 100%)". This line shows the effect of chemotherapy in the presence of radiotherapy, corrected for the effect of radiotherapy only, whereas the "chemo + radiotherapy (no radiotherapy = 100%)" line shows the overall effect of this combination therapy on tumoroid viability, compared with no treatment. **L** and **M,** The effect of chemotherapy (cisplatin or cetuximab) on radiotherapy sensitivity in organoids. AUC is shown as indicator of organoid sensitivity to *in vitro* radiotherapy. For each line tested, AUC is shown for radiotherapy alone, or when combined with chemotherapy. Here, the effect of radiotherapy is corrected for the effect of chemotherapy alone. As such, the green area indicates lines where chemotherapy serves as a radiosensitizer, whereas the red area indicates lines where chemotherapy acts as a radioprotector.

was given after excision of the primary tumor. Indications for adjuvant radiotherapy included close surgical margins and positive sentinel node. The patient received a total dose of ionizing radiation of 56 Gy and was last seen 2 months after the end of treatment. So far, there are no signs of recurrence. It is too early to tell if this patient will remain in remission. It will be of interest to see whether disease will recur, because based on our *in vitro* findings, radiotherapy should have been effective for this particular tumor. Finally, although T8 appeared resistant to radiotherapy in the *in vitro* assay, patient T8 so far has not shown relapse after treatment. The patient received adjuvant radiotherapy after incomplete resection of a gingival SCC (stage T4aN0). A dose of 66 Gy was delivered to the tumor area. Five months later, no signs of recurrence were observed upon physical examination. Standard follow-up

is ongoing. It will be of interest to see whether the patient relapses in the coming months, a progression that would be in line with our *in vitro* findings.

Combination of Chemotherapy and Radiotherapy in HNSCC-Derived Organoids Allows the Study of Synergistic Effects of These Therapies

In an attempt to overcome the observed radioresistance, HNSCC organoids that were responding poorly to radiotherapy were reexposed to radiation, but now in the presence of LC161. LC161 is a Second Mitochondria-derived Activator of Caspase (SMAC) mimetic, described to overcome intrinsic cell death resistance by promoting degradation of cellular inhibitor of apoptosis proteins (56). As others have shown an effect of SMAC mimetics in HNSCC cells, either alone or in

combination with radiotherapy, we set out to test this in HNSCC organoids (57). Indeed, a radio-sensitizing effect of LC161 was observed in T8. In parallel, T1 and T9 were also tested, but did not show increased sensitivity to radiotherapy in the presence of LC161. In T8 organoids, the addition of SMAC mimetic increased cell death in response to radiation (Fig. 6H). Importantly, LC161 did not radiosensitize the matched N8 organoids; these were more resistant to this treatment. To validate these findings and understand which type of cell death was triggered in response to radiotherapy combined with LC161, the treatment was repeated in the presence of either Z-VAD-FMK (zVAD) or Necrostatin1 (Nec1), which block apoptosis or necroptosis, respectively. It was found that the addition of Nec1, but not zVAD-FMK, could prevent the radiosensitizing effect of the SMAC mimetic (Fig. 6I). These findings show that T8 tumor cells, in line with general tumorigenic mechanisms (58), evade apoptosis, yet that this resistance could be overcome by the addition LC161. These results highlight the potential of organoids to explore alternative (sensitizing) therapies on a personalized level.

In addition to determining radiosensitivity of the tumoroids, we set up an *in vitro* screening assay combining chemotherapy with radiotherapy. We exposed organoids to a gradient of chemotherapy in the presence (2 Gy) or absence (0 Gy) of radiation. Previously detected differences in sensitivity for these compounds were confirmed (cetuximab sensitivity T5 > T8, cisplatin sensitivity T2 > T1; Fig. 6J and K). We found that combination therapy resulted in increased cell death at lower doses of chemotherapy than when chemotherapy was given as a single agent. To study the effect of chemotherapy in the presence of radiation, we compared organoids treated with chemotherapy and radiotherapy with organoids exposed to radiotherapy alone (T5 and T8 to cetuximab, T1 and T2 to cisplatin; Fig. 6J and K). It seems that in these cases, the effect of chemotherapy itself is not changed by the presence of radiotherapy, although the combination treatment results in additional cell death.

Using the same approach, we studied the radiosensitizing effect of chemotherapy *in vitro*. In the clinic, such combination therapy is used to treat patients with HNSCC, in both the curative and adjuvant setting. The combination of cisplatin or cetuximab with radiotherapy increases relapse-free survival when compared with treatment with radiotherapy alone in clinical trials (59). Because radiotherapy and chemotherapy are given concurrently to patients, it is impossible to understand whether the effect between these treatments is additive or synergistic. Here, 10 organoid lines (T1–T6, T8, T24, T25, and T27) were exposed to a range of radiotherapy, in either the presence or absence of a toxic dose of cisplatin or cetuximab. Indeed, the combination of chemotherapy and radiotherapy resulted in increased cell death when compared with single-agent treatment. When corrected for the effect of the chemotherapy itself, sensitivity to radiotherapy was increased in the presence of cisplatin in six of ten tested lines, and in four of ten when combined with cetuximab (Fig. 6L and M; Supplementary Fig. S14A). Although not statistically significant, a correlation between the effect of radiotherapy alone and radiotherapy combined with cisplatin was observed. Overall, response to radiotherapy improved in the presence of cisplatin, implying a synergistic effect (Supplementary Fig. S14B). On the basis of the data presented here, this is not the

case when radiotherapy is combined with cetuximab (Supplementary Fig. S14C). This suggests that, although additive (Supplementary Fig. S14D and S14E), no synergistic effect of cetuximab and radiotherapy can be observed, at least *in vitro*.

HNSCC Organoids as a Platform to Identify Effective Targeted Therapies

On the basis of mutations detected in this set of HNSCC-derived tumoroids, we determined the *in vitro* sensitivity for a range of targeted therapies that are not used in the treatment of patients with HNSCC. As T1, T7, T9, T10, T24, T25, and T29 carry activating mutations in *PIK3CA*, sensitivity to the PIK3CA inhibitor alpelisib was determined for sequenced tumoroid lines eligible for drug screening (Supplementary Fig. S12). *PIK3CA* mutation has been investigated as a biomarker for response to PIK3CA inhibitors (60–62). Although some studies imply that activating mutations of *PIK3CA* can serve as a biomarker for good response, others claim the type of mutation can influence response to these therapeutics. We observe no enrichment for *PIK3CA* mutations in the organoid lines more responsive to alpelisib (Fig. 7A). Recently, a study linking genetic alterations to alpelisib responses in patients showed that patients carrying H1047R *PIK3CA* mutations had a more durable response in the clinic, whereas a negative association was found between E545K mutations and alpelisib response (62). When testing all *PIK3CA*-mutant organoid lines eligible for drug screening, T9 organoids (*PIK3CA* H1047R, IC$_{50}$ 0.32 μmol/L) showed increased sensitivity to alpelisib compared with the E545 PIK3CA–mutant organoids T1 (IC$_{50}$ 3.19 μmol/L) and T7 (IC$_{50}$ 2.69 μmol/L). However, the IC$_{50}$ value of organoid line T25, also carrying a H1047R activating mutation in *PIK3CA*, was 2.01 μmol/L (Fig. 7B). Although still lower than the IC$_{50}$ values obtained for the E545K-mutant organoid lines, these data support the hypothesis that *PIK3CA* mutation status cannot predict response to PIK3CA inhibitors in all cases, and functional testing might be required to identify responders.

BRAF V600E mutations were detected in T9 and T10. Therefore, we tested a panel of tumoroid lines for sensitivity to vemurafenib, a BRAF inhibitor (Fig. 7C). As expected, we observed increased sensitivity of *BRAF*-mutant T9 when compared with the other tumoroid lines tested in this assay.

Finally, we exposed the panel of tumoroids to the PARP inhibitor niraparib, the mTOR inhibitor everolimus, and the FGFR inhibitor AZD4547 (Fig. 7D–F). These compounds were selected on the basis of the genetic alterations described in HNSCC (30). Interestingly, although mutations in *PARP, MTOR,* and *FGFR* were not detected in the characterized tumoroid lines, we observed variable sensitivities to these compounds (Supplementary Fig. S12). For all tested compounds, the difference in response between matched normal and tumor organoids was tested (Supplementary Fig. S15). Responses to therapies remained stable over time (Supplementary Fig. S16). Among the lines sensitive to everolimus (Fig. 7D) was tumor line T27, which carries a RET mutation. Inhibition of mTOR signaling has been shown to inhibit the growth of RET-mutant tumor cells *in vitro* (63). AZD4547 was also found to effectively target tumoroid line T27 (Fig. 7E). This response can likely be explained by the mutation in KDR (also known as VEGFR2A) detected in T27 organoids. Indeed, AZD4547 has been shown to target KDR
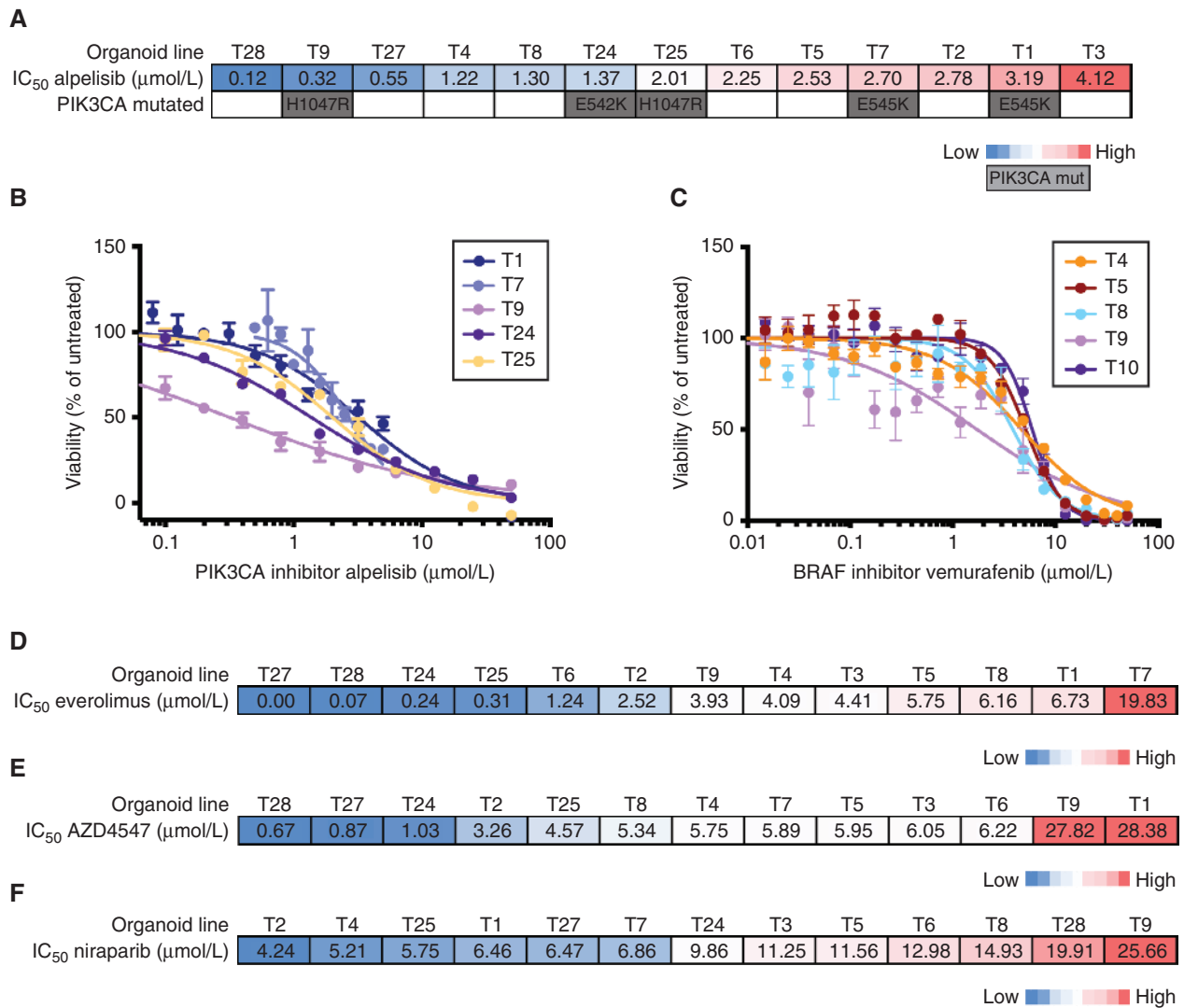
Figure 7. HNSCC organoids as a platform to identify effective targeted therapies. **A,** Heat map showing IC$_{50}$ values of tumoroid lines exposed to PIK3CA inhibitor alpelisib. Red indicates high IC$_{50}$ values, blue indicates low IC$_{50}$ values. Amino acid changes caused by the respective genetic alterations are shown in the row below to highlight that mutation status is not correlating to alpelisib response. **B,** Sensitivity of tumoroid lines T1, T7, T9, T24, and T25 for PIK3CA inhibitor alpelisib. **C,** Sensitivity of tumoroid lines T4, T5, T8, and T9 for BRAF inhibitor vemurafenib. T9 (carrying a *BRAF* V600E activating mutation) shows increased sensitivity to this agent. **D,** Heat map showing IC$_{50}$ values of tumoroid lines exposed to mTOR inhibitor everolimus. Red indicates high IC$_{50}$ values, blue indicates low AUC values. **E,** Heat map showing IC$_{50}$ values of tumoroid lines exposed to FGFR inhibitor AZD4547. Red indicates high IC$_{50}$ values, blue indicates low AUC values. **F,** Heat map showing IC$_{50}$ values of tumoroid lines exposed to PARP inhibitor niraparib. Red indicates high IC$_{50}$ values, blue indicates low AUC values.

in addition to FGFR1, although with lower affinity (64). Taken together, these data reveal differences in sensitivity to all compounds tested between different tumoroid lines, which in some, but not all, cases can be explained by detected genetic alterations. Thereby, these data illustrate the potential of this technology to guide personalized therapy in the future.

DISCUSSION

We present a protocol for long-term expansion of wild-type oral mucosal epithelia and HNSCC in the form of organoids. The growth factor cocktail that is used in this work differs from that for other epithelia. The addition of the GSK3ß

inhibitor CHIR and the growth factor FGF2 appears essential for the successful establishment of these organoids. We characterize HNSCC organoids by histology, gene-expression analysis and, in the case of tumoroids, by mutational profiling. Using the technique described here, we can retain normal keratinocytes without the requirement for feeder cells in culture for >15 passages. To document that these organoids are amenable to infectious disease modeling, we performed infection with HSV1 and HPV16. Previous studies have applied 3-D models of fibroblasts, vaginal epithelium, and melanoma cells to study the interaction of HSV1 with epithelial cells (65, 66). Yet to our knowledge a 3-D model to study HSV1 infection in oral mucosa cells has not been reported. Infection

with HPV16 has been limited to studies in immortalized cell lines, or to primary cells that can be cultured only briefly (21). Essential for HPV infection is viral access to basal cells of the stratified epithelium, whereas for virion production, differentiated keratinocytes are essential. A model that retains this stratification *in vitro* and shows productive infection, such as the one described here, should therefore be valuable to research in this field.

We report the initiation of an HNSCC-derived organoid biobank, which is being expanded significantly. Like our other biobanks, these will be made available to the research community. The biobank was used to test sensitivity to a panel of drugs. This drug panel included both drugs currently used in the treatment of patients with HNSCC and targeted drugs that based on their molecular targets appeared relevant to be tested in this setting. The fact that a variable response to cisplatin, carboplatin, cetuximab, and radiotherapy was observed *in vitro* suggests that this method records interindividual differences. This implies that tumor-derived HNSCC organoids hold potential to guide personalized therapy. Vlachogiannis and colleagues recently showed the predictive potential of similar drug screens using organoids derived from metastasized gastrointestinal cancers (23).

The high take rate and the fast growth rate of the HNSCC tumoroids makes them particularly suited for personalized approaches. In current clinical practice, treatment options for HNSCC are dictated by site, stage, and patient factors. There is a need for more tailored treatment. For this reason, we explored the potential to correlate organoid responses to patient outcome. Clinical data were available for 7 patients who presented with tumors in different anatomic locations. They received different total dosages of radiotherapy, while all were therapy-naïve at the start of treatment. Although numbers should still be considered small, we find that clinical response of patients treated with radiotherapy can be correlated to *in vitro* responses of the corresponding organoids. To investigate whether such a correlation truly exists, more cases are required, especially considering the heterogeneity of this disease and other variables that influence patient outcome (total delivered dose, if surgery is performed and, if so, if resection is successful, ability to finish treatment regimen as prescribed, etc.). To follow up on these initial findings, we are embarking on an observational study to link patient outcome to organoid responses *in vitro* (ONCODE-P2018-0003). We anticipate including approximately 80 patients. Organoids will be exposed to cisplatin, carboplatin, or cetuximab, and combined with irradiation such as occurs in clinical practice. Here, we already show the possibility of combining chemotherapy and radiotherapy *in vitro*. The observational trial will elucidate whether these *in vitro* results hold predictive potential for patient responses.

Cetuximab is used in the treatment of patients with HNSCC. Fifty percent to 90% of tumors overexpress EGFR (47), and 15% carry gene amplification of *EGFR* (30). Initially, it was expected that differing levels of EGFR expression could explain patient response to anti-EGFR therapy. However, it has been shown that neither EGFR overexpression nor increased gene copy number can serve as a prognostic biomarker for cetuximab response (47). In agreement, the cetuximab sensitivity of the tumoroids could not be correlated by their EGFR expression levels. It will be interesting to

see whether this correlation can be observed in larger panels of patient-derived organoids. A direct, functional test such as offered by patient-derived tumoroids may prove valuable.

Because chemotherapy and radiotherapy are given concurrently to patients, it is difficult to evaluate the effect of these single treatments at the individual patient level. As shown here, organoids can be used to study the effect of these treatments as single agents, but also can be used to study how chemotherapy influences radiotherapy efficacy and vice versa. As such, our results suggest that cetuximab does not act as a radiosensitizer in patient-derived HNSCC cells. Regardless, compared with radiotherapy alone, the combination of cetuximab and radiotherapy results in increased cell death *in vitro*, fitting with clinical data (67).

In addition, screening for sensitivity to other targeted drugs may be of value when the tumor recurs. The targeted therapies tested in our studies (everolimus, niraparib, alpelisib, AZD4547, and vemurafenib) yielded differential responses. Although phase I and II clinical trials are ongoing to test a number of these drugs in patients with HNSCC (68–70), implementation remains limited. Organoids might serve as an *in vitro* tool to select the right therapy for the right patient. Alternatively, studying the characteristics of those organoids that are responding in such screens might help identify biomarkers that distinguish responders from nonresponders. As an example, in this study we show that *PIK3CA*-mutant tumoroid lines show variable responses to alpelisib. *PIK3CA* E545K–mutant lines showed a similar response to the other *PIK3CA* wild-type tumoroids in our panel, whereas H1047R-mutant lines showed increased sensitivity to this agent (although the extent of sensitivity differed for the two H1047R-mutant lines tested here). In patients, differences in alpelisib responses could indeed be linked to the type of *PIK3CA* mutation, where H1047R-mutant patients showed more durable responses than patients harboring a E545K mutation (62). On the contrary, other studies have implicated *PIK3CA* mutation as a predictor for alpelisib response, regardless of the specific mutation (60, 61). Our data support the hypothesis that the type of *PIK3CA* mutation might be relevant for the response to alpelisib. In organoids, the presence of *PIK3CA* activating mutations did not correlate with *in vitro* responses to alpelisib. These differences in sensitivity between lines carrying identical *PIK3CA* mutations might be explained by other genetic alterations, interfering with the dependence on this pathway for cell survival.

In vitro responses observed in this study could in some, but not all, cases be explained by the genetic alterations detected in the tumoroid lines. For example, the response of tumoroid line T27 to AZD4547 can be explained by the mutation in KDR, as AZD4547, designed as an FGFR inhibitor, is known to also target KDR with high affinity (64). Interestingly, in the panel tested here, there are tumoroid lines showing comparable sensitivity to this therapeutic agent, although at this point we cannot identify genetic alterations explaining this sensitivity. These results indicate that, at least in some cases, functional tests such as those performed here might be more informative than genetic screening to predict response to therapeutic agents.

In an attempt to detect general therapy resistance mechanisms, we performed differential gene expression on a panel

of organoid lines that responded either well or poorly to cisplatin/carboplatin, cetuximab, or radiotherapy. Under current conditions (sequencing depth, number of samples included in the analysis, etc.), no indications for resistance mechanisms could be deduced from this data by gene enrichment analysis. Differently expressed gene lists did contain genes previously described to be associated with therapy resistance. For example, genes enriched in radiotherapy-resistant organoid lines included *PGK1* and *GPX3*. For both genes, high expression has previously been associated with poor response to radiotherapy or DNA-damaging therapies (52, 53). Expression of *IGFBP5* and *SLC16A3*, both enriched in cetuximab-resistant organoid lines, have previously been reported to be biomarkers for poor response to cetuximab (54, 55).

Finally, extension of this system to the generation of immune-tumoroids, tumor-derived organoids combined with immune cells, might make this system suitable to test responses to immunomodulating antibodies. Such drugs are currently evaluated in patients with HNSCC (71). Again, prognostic biomarkers are largely lacking. Initial studies demonstrate that tumoroids can be cocultured with immune cells (derived from either peripheral blood or tumor microenvironment) and can provide functional readouts (17, 72).

METHODS

Human Material for Organoid Cultures

The collection of patient data and tissue for the generation and distribution of organoids has been performed according to the guidelines of the European Network of Research Ethics Committees (EUREC) following European, national, and local law. The Biobank Research Ethics Committee of the University Medical Center Utrecht (TCBio) approved the biobanking protocol: 12-093 HUB-Cancer according to the University Medical Center Utrecht (UMCU) Biobanking Regulation. All donors participating in this study signed informed-consent forms and can withdraw their consent at any time, leading to the prompt disposal of their tissue and any derived material, as well as the cessation of data collection. Available organoids will be cataloged at www.hub4organoids.eu and can be requested at info@hub4organoids.eu.

Tissue Processing

Patient material was collected from pathology material in Advanced DMEM/F12 (Life Technologies, catalog no. 12634-034), supplemented with 1× GlutaMAX (adDMEM/F12; Life Technologies, catalog no. 12634-034), Penicillin–streptomycin (Life Technologies, catalog no. 15140-122), and 10 mmol/L HEPES (Life Technologies, catalog no. 15630-056). This medium was named Advanced DMEM +/+/+. For collection of patient material, 100 µg/mL Primocin (Invivogen, catalog no. ant-pm1) was added to the +/+/+ medium. For normal tissue samples, excess fat or muscle tissue was removed to enrich for epithelial cells, and tissue was cut into small fragments. Random pieces of approximately 5 mm³ were stored at −20°C for DNA isolation. Some pieces were fixed in formalin for histopathologic analysis and IHC, and the remainder was processed for organoid derivation. Fragments were incubated at 37°C in 0.125% Trypsin (Sigma, catalog no. T1426) in +/+/+ until digested. Every 10 minutes, the tissue suspension was sheared using 1 mL pipette. Digestion was monitored closely to prevent excess incubation in trypsin. Incubation was performed for a maximum of 60 minutes. When complete, Trypsin was diluted by addition of 10 mL +/+/+. Suspension was strained over a 100 µm EasyStrainer filter (Greiner, catalog no. 542000) and centrifuged at 1,000 rpm. The resulting pellet was resuspended in ice-cold 70% 10 mg/mL cold Cultrex growth factor–reduced BME type 2 (Trevigen, 3533-010-02) in organoid medium. Droplets of approximately 10 µL were plated on the bottom of preheated suspension culture plates (Greiner, catalog no. M9312). After plating, plates were inverted and put at 37°C for 30 minutes to let the BME solidify. Subsequently, prewarmed organoid medium was added to the plate. For the first week, 10 µmol/L Rho-associated kinase (ROCK) inhibitor Y-27632 (Abmole Bioscience, catalog no. M1817) was added to the medium to aid outgrowth of organoids for the primary tissue. For mouse-derived organoids, tongue tissue was obtained from control mice used under Instantie voor Dierenwelzijn (IvD)–approved projects. Subsequent processing of tissue was identical to processing of human tissue.

Organoid Culture

HNSCC and normal epithelium-derived organoids were grown in Advanced DMEM +/+/+. Organoid medium contained 1 × B27 supplement (Life Technologies, catalog no. 17504-044), 1.25 mmol/L N-acetyl-L-cysteine (Sigma-Aldrich, catalog no. A9165), 10 mmol/L Nicotinamide (Sigma-Aldrich, catalog no. N0636), 50 ng/mL human EGF (PeproTech, catalog no. AF-100-15), 500 nmol/L A83-01, 10 ng/mL human FGF10 (PeproTech, catalog no. 100-26), 5 ng/mL human FGF2 (PeproTech, catalog no. 100-18B), 1 µmol/L Prostaglandin E2 (Tocris Bioscience, catalog no. 2296), 0.3 µmol/L CHIR 99021 (Sigma-Aldrich, catalog no. SML1046), 1 µmol/L Forskolin [Bio-Techne (R&D Systems) catalog no. 1099], 4% R-spondin, and 4% Noggin (both produced via the r-PEX protein expression platform at U-Protein Express BV). Mouse organoids were maintained similar to human organoids, but were grown in +/+/+, containing B27, 25 mmol/L N-acetyl-L-cysteine, 10 mmol/L Nicotinamide, 2% RSPO, 50 ng/mL EGF, and 10 ng/mL FGF10. Organoids were split between 7 and 14 days after initial plating. For passaging, organoids were collected from the plate by disrupting the BME droplets with a P1000, collecting and washing in 10 mL +/+/+. Pellet was resuspended in 1 mL of TrypLE Express (Life Technologies, catalog no. 12605-010) and incubated at 37°C. Digestion was closely monitored and suspension was pipetted up and down every 5 minutes to aid disruption of the organoids. TrypLE digestion was stopped when organoids were disrupted into single cells by adding 10 mL +/+/+. Cells were subsequently resuspended in ice-cold 70% BME in organoid medium and plated at suitable ratios (1:5 to 1:20) to allow efficient outgrowth of new organoids. After splitting, 10 µmol/L Y-27632 was always added to aid outgrowth of organoids from single cells. Medium was changed every 2–3 days and organoids were split once every 1–2 weeks.

RNA Collection

Organoids were cultured as normal. For differentiation of the organoids (as shown in Fig. 1C), organoids were split to single cells, left to grow one week on organoid medium, and then put on +/+/+ for one week before collection. On the day of collection, organoids were collected from tissue culture plates and washed twice in 10 mL +/+/+. RNA was extracted using RNeasy Mini Kit (Qiagen, catalog no. 74104) according to protocol. RNA amount was measured using NanoDrop. For quantification of *EGFR* expression, organoids were split to single cells, left to grow 5 days on organoid medium, and then put on organoid medium with lower EGF concentration (0.63 ng/mL).

RNA Sequencing

RNA was processed as described previously, following the protocol of CEL-Seq (73, 74). Paired-end sequencing was performed on the Illumina Nextseq500 platform, High Output 2 × 75 bp run mode. Read 1 was used to identify the Illumina library index and CEL-Seq sample barcode. Read 2 was aligned to the hg19 human RefSeq transcriptome using BWA (75). Reads that mapped equally well to multiple locations were discarded. Around 2 million reads were mapped per sample. Samples with low number of reads were removed. Sample

annotation and barcodes can be found on the GEO submission of this data. The remaining samples were normalized and analyzed by the DESeq2 package (32). For visual comparison between samples, regularized log transformed (rlog) values were used.

cDNA Synthesis and Quantitative PCR

For cDNA synthesis, RNA was incubated with 50 μg/mL Oligo (dT) 15 Primer (Promega, catalog no. C1101) in water for 5 minutes at 70°C. Subsequently GoScript Reverse Transcriptase (Promega, catalog no. A5003) was used according to protocol to produce cDNA. qPCR reactions were performed in 384-well format using IQ SYBR green (Bio-Rad, catalog no. 1708880) in the presence of 0.67 μmol/L forward and reverse primer and cDNA transcribed from 25 ng RNA. For qPCR, samples were incubated for 2 minutes at 95°C and for 40 cycles at: 15 seconds at 98°C, 15 seconds at 58°C, and 15 seconds at 72°C. Results were calculated by using the $\Delta\Delta C_t$ method. Expression was calculated relative to expression in tongue tissue (total RNA, human normal tongue tissue, AmsBio, catalog no. R1234267). Melt peak analysis was performed to assure that primer had no aspecific binding. Primers used were the following:

Human p63 forward: GACAGGAAGGCGGATGAAGATAG,
Human p63 reverse: TGTTTCTGAAGTAAGTGCTGGTGC,
Human Ki-67 forward: GAGGTGTGCAGAAAATCCAAA,
Human Ki-67 reverse: CTGTCCCTATGACTTCTGGTTGT,
Human KRT13 forward: GACCGCCACCATTGAAAACAA,
Human KRT13 reverse: TCCAGGTCAGTCTTAGACAGAG,
Human KRT4 forward: CTCTTTGAGACCTACCTCAGTGT,
Human KRT4 reverse: GGCTGCTGTGCGTTTGTTG,
Human EGFR forward: AGGCAGGAGTAACAAGCTCAC,
Human EGFR reverse: ATGAGGACATAACCAGCCACC,
Human Actin forward: TGCGTGACATTAAGGAGAAG,
Human Actin reverse: TGAAGGTAGTTTCGTGGATG,
Human GAPDH forward: GGAGCGAGATCCCTCCAAAAT,
Human GAPDH reverse: GGCTGTTGTCATACTTCTCATCG.

DNA Isolation

DNA was isolated using Reliaprep gDNA Tissue Miniprep System (Promega, catalog no. A2052) according to protocol. DNA concentration were measured using NanoDrop.

Growth Rate Analysis

Single cells (100,000) were plated in 50 μL of BME. After one week in culture, all organoids were collected and disrupted into single cells. Cells were counted and total cell number was determined. Counting was performed four times. By calculating the number of cells at day 7, which all came from the 100,000 cells plated at day 0, a multiplication factor could be determined for each week. Using this, a theoretical total number of cells could be calculated by multiplying the total cell number of the previous week with the multiplication factor of that week. Subsequently, 100,000 of the counted single cells were plated in 50 μL BME. This procedure was repeated for five weeks.

HSV Infection and Quantification Experiments

For imaging experiments, cells were incubated with 1×10^7 PFU HSV-dTomato virus in the culture medium. The virus was a kind gift of Prashant Desai (John Hopkins University, Baltimore, MD). For DNA quantification, organoids were split using TrypLE. On the third day after splitting, organoids were incubated with 1×10^7 PFU HSV-dTomato virus in suspension for 6 hours. After washing with 10 mL +/+/+, organoids were plated (1,500 organoids in 20 μL BME per well) in 48-well format. Organoids were kept in organoid medium, with or without 10 μmol/L acyclovir (Sigma). For DNA collection, the BME drop was collected together with culture medium and added to 10 mL +/+/+ in a 15 mL falcon tube. After centrifugation, medium

was removed and pellet was stored at −20°C until gDNA extraction. For DNA quantification, qPCR reactions were performed in 384-well format using IQ SYBR Green Mix (Bio-Rad) in the presence of 0.67 μmol/L forward and reverse primer and 2% of total DNA isolated from 1,500 organoids. After gDNA extraction, qPCR was performed with the following primers to detect HSV DNA: forward: 5′-ATCAACTTC GACTGGCCCTT-3′ and reverse: 5′-CCGTACATGTCGATGTTCAC-3′. PCR program used: 2 minutes at 95°C and for 40 cycles at: 15 seconds at 98°C, 15 seconds at 60°C, and 15 seconds at 72°C. Increase in DNA content was calculated relative to noninfected wells.

HPV Infection and Quantification Experiments

HPV16 virions were produced as described previously (26). Upon fractionation of the supernatant containing the virus, fractions with highest titer (as determined by quantitative PCR on HPV DNA) were pooled and subsequently used for infection experiments. Organoids were split using TrypLE and plated at a density of 1,500 cells/well, in 20 μL BME drops. After the addition of culture media, HPV-containing supernatant was added to the wells. During the course of the experiment, medium was refreshed every 2–3 days. DNA isolation and DNA quantification were performed as described for HSV infections, except primers used were: forward: 5′-CTACATGGCATTGGACA GGA-3′ and reverse: 5′-GGTCACGTTGCCATTCACTA-3′. For reinfection experiments, supernatant taken from organoids cultured for 12 days after HPV infection was collected and filtered with 0.45-μm pore filter. Subsequently, this was added to the uninfected organoids.

Next-Generation Sequencing

Oncopanel sample prep and analysis was performed as described previously (76) and sequenced with the mpliSeq Cancer Hotspot Panel V2+ (for details: https://www.umcutrecht.nl/getmedia/ c39cd469-a4de-4ae9-9a52-0b8ed6761311/CHPv2Plus_NGS.pdf. aspx). For sample T27, an extended oncopanel was used, where 140 genes were checked with 3,817 probes targeting a region of 1,080,437 bp. For library preparation, SureSelectXT Library Prep Kit was used following the SureSelectXT Target Enrichment System for Illumina Version B.2 protocol. For cluster generation, the library is loaded into a flow cell where fragments are captured on a lawn of surface-bound oligos complementary to the library adapters. Each fragment is then amplified into distinct, clonal clusters through bridge amplification. Total reads were above 50,000,000 (52 < GC% > 50).

Whole-exome sequencing data were mapped against human reference genome GRCh37, and variants were called using the IAP pipeline (https://github.com/UMCUGenetics/IAP). To obtain high-quality somatic mutation catalogs, we filtered out variants with evidence in their corresponding normal samples, overlaps with the single nucleotide polymorphism database v137.b3730, and the variants did not reach our quality measurements (base coverage of 10×, VAF of 0.1, GATK phred-scaled quality score of 100 for base substitutions, 250 for indels and mapping quality of 60 for indels). Indels that were present within 100 bp of a called variant in the control were excluded. Only autosomal variants were considered. The scripts used for the filtering are available at: https://github.com/UMCUGenetics/SNVFI, and https://github.com/ ToolsVanBox/INDELFI. Nonsynonymous mutations (missense mutation, start loss, stop gain, in-frame insertion/deletion, and frame shift) in the genes checked in the OncoPanel were reported as driver mutations. Whole-exome sequencing data has been deposited in the European Genome–Phenome Archive (EGA; https://www.ebi.ac.uk/ ega/home); accession number EGAS00001003628.

In Vitro Drug Screen

Two days prior to start of the drug screen, organoids were passaged and disrupted into single cells using TrypLE. Single cells were plated in 70% BME in organoid medium as for regular splitting. Two

days later, organoids were collected from the BME by the addition of 1 mg/mL dispase II (Sigma-Aldrich, catalog no. D4693) to the medium of the organoids. Organoids were incubated for 30 minutes at 37°C to digest the BME. Subsequently, organoids were filtered using a 70-mm nylon cell strainer (BD Falcon), counted, and resuspended in 5% BME/growth medium (12,500 organoids/mL) prior plating in 40 μL volume (Multi-drop Combi Reagent Dispenser, Thermo Scientific, catalog no. 5840300) in 384-well plates (Corning, catalog no. 4588).

The drugs were added 1 hour after plating the organoids using the Tecan D300e Digital Dispenser (Tecan). Nutlin-3 (Cayman Chemical, catalog no. 10004372), Niraparib (Selleckchem, catalog no. S2741), AZD4547 (ApeXbio, catalog no. A8250), everolimus (LC Laboratories, catalog no. E4040), vemurafenib (Selleckchem, catalog no. S1267), and alpelisib (LC Laboratories, catalog no. A4477) were dissolved in DMSO. Cisplatin (Sigma, catalog no. C2210000), carboplatin (Sigma, catalog no. C2538), and cetuximab (obtained from hospital pharmacy) were dissolved in PBS containing 0.3% Tween-20, which was required to dispense these drugs using the HP printer. All wells were normalized for solvent used. DMSO percentage never exceeded 1%, PBS/Tween-20 percentage never exceeded 2%. Drug exposure was performed in triplicate for each concentration shown. For a layout of the drug screen, see Supplementary Fig. S12.

One hundred twenty hours after adding the drugs, ATP levels were measured using the CellTiter-Glo 3-D Reagent (Promega, catalog no. G9681) according to the manufacturer's instructions, and luminescence was measured using a Spark multimode microplate reader (Tecan). Results were normalized to vehicle (100%) and baseline control (Staurosporin 1 μmol/L; 0%). For each line, when viability did not go above 70% or below 30%, an additional screen was performed for that particular drug with an adjusted dose of this drug for this organoid line. Screen quality was determined by checking Z factor scores for each plate following this formula:

$$Z \text{ factor} = 1 - \frac{3 \times \text{SD (negative control)} + 3 \times \text{SD (positive control)}}{\text{Average (negative control)} - \text{average (positive control)}}$$

Drug screens with a Z factor of <0.3 were not used and repeated. Kill curves were produced using GraphPad software and lines were fitted using the option "log (inhibitor) versus normalized response-variable slope."

Radiation of Organoids

Organoids were disrupted into single cells using TrypLE, and plated at a density of 6,000 single cells in 30 μL BME drops in a 48-well plate. Two days later, cells were irradiated. For each radiation dose, a separate plate was used. Plates were sealed air-tight and irradiated with a single fraction of 0–8 Gy using a linear accelerator (Elekta Precise Linear Accelerator 11F49, Elekta). The plates were positioned on top of 2-cm polystyrene and submerged in a 37°C water bath. After radiation, medium was changed. Four days later, readout was performed as described previously.

Chemoradiation Therapy in Organoids

For testing a range of chemotherapy concentrations in the presence or absence of radiotherapy, drug screens were performed as described in the section "*In vitro* drug screen." Two identical plates of organoids were treated with the desired chemotherapy. One day after the start of treatment, one of these plates was irradiated with a total dose of 2 Gy. This dose was chosen as a sublethal dose based on the radiotherapy-only experiments that were previously performed.

To test a range of radiation doses in the presence or absence of cisplatin, cetuximab, LC161, zVAD-FMK, or Necrostatin 1, organoids were disrupted into single cells using TrypLe, and plated at a density of 6,000 organoids per 20 μL BME in 96-well plates. One day later, chemotherapy treatment was started. On the basis of chemotherapy screens that were previously performed, the sublethal

doses of 5 μmol/L cisplatin and 30 μg/mL cetuximab were chosen. On the basis of literature, 1 μmol/L LC161, 10 μmol/L zVAD, and 10 μmol/L Necrostatin were used. One day later, cells were irradiated as described above. Four days later, readout was performed.

Live-Cell Imaging and Lentiviral Infection

Organoids were infected with lentivirus encoding mNeon-tagged histone 2B and a puromycin-resistant cassette (77). After selection, organoids were plated in BME in glass-bottom 96-well plates and mounted on an inverted confocal laser scanning microscope (Leica SP8X), which was continuously held at 37°C and 5% CO_2. Over 16 to 20 hours, approximately 10 H2B-mNeon–expressing organoids were imaged simultaneously in XYZT mode using a ×40 objective (N.A. 1.1), using minimal amounts of 506 nm laser excitation light from a tunable white light laser. Time interval was approximately 3 minutes (2:30–3:20 minutes). Cell divisions were scored, judged, and counted manually.

Transplantations

For all *in vivo* work, ethical approval was gained prior to the start of this project by the Central Authority for Scientific Procedures on Animals (CCD) and the local animal experimental committee at the Hubrecht Institute (IvD-HI-KNAW-HI 17.10.11). Five days before transplantation, organoids were disrupted to single cells and plated as usual. On the day of transplantation, organoids were disrupted into single cells and resuspended in 50% BME/organoid medium at a density of 33.33 million cells per mL. Cells (2.5 million) were subcutaneously injected in *NOD.Cg-Prkdc*scid *Il2rg*tm1Wjl/*SzJ* mice between 6 and 12 weeks of age. Six weeks after injection, mice were sacrificed by cervical dissociation, and tumors were excised and fixed overnight in 4% formaldehyde.

IHC

Tissues or organoids were fixed in 4% paraformaldehyde overnight, dehydrated, and embedded in paraffin. Sections were subjected to H&E as well as IHC staining. The details on primary antibodies used for IHC staining on organoids and primary tissue are given in Supplementary Table S7. Staining for TP40, TP53, MKI67, and KRT5 on the tumoroids (Fig. 2) was performed at the pathology department of the UMCU (Utrecht, the Netherlands).

Karyotyping

Two days after splitting, organoids were treated with 0.1 μg/mL Colcemid (Gibco 15212012) for 17 hours in organoid medium. After that, organoids were disrupted into single cells using TrypLE and processed as described previously (78). Metaphase spreads were mounted with DAPI-containing VectaShield (Vector Laboratories, catalog no. H-1200) and imaged on a DM6000 Leica microscope.

Scanning Electron Microscopy

Organoids were collected and BME was removed using Cell Recovery Solution (Corning). To fix organoids, 1 mL of 1% (v/v) glutaraldehyde (Sigma-Aldrich, G5882) in PBS was added. After overnight fixation at 4°C, organoids were transferred onto 12-mm coverslips (Corning, catalog no. 354085). Samples were dehydrated by consecutive 10-minute incubations in 2 mL of 10% (v/v), 25% (v/v), and 50% (v/v) ethanol-PBS, 75% (v/v) and 90% (v/v) ethanol-H_2O (2x) followed by 50% ethanol-hexamethyldisilazane (HMDS), and 100% HMDS (Sigma-Aldrich, catalog no. 379212). Coverslips were removed from the 100% HMDS, air-dried overnight at room temperature, and mounted onto 12-mm specimen stubs (Agar Scientific). After gold-coating to 1 nm using a Q150R sputter coater (Quorum Technologies), samples were examined with a Phenom PRO table-top scanning electron microscope (Phenom-World).

Transmission Electron Microscopy

Organoids were placed in BME on 3-mm diameter and 200-μm depth standard flat carriers for high-pressure freezing and immediately cryoimmobilized using a Leica EM high-pressure freezer (equivalent to the HPM10), and stored in liquid nitrogen until further use. They were freeze-substituted in anhydrous acetone containing 2% osmium tetroxide 0.1% uranyl acetate at –90°C for 72 hours and warmed to room temperature, 5°C per hour (EM AFS-2, Leica). The samples were kept 2 hours at 4°C and 2 additional hours at room temperature. After acetone rinses (4 × 15 minutes), Epon resin infiltration was performed during 2 days (acetone: resin 3:1, 3 hours; 2:2, 3 hours; 3:1, overnight; pure resin: 6 hours + overnight + 6 hours + overnight + 3 hours). Resin was polymerized at 60°C during 96 hours. Leica Ultracut UC6 ultramicrotome was used to cut sections that were mounted on Formvar-coated copper grids and stained with 2% uranyl acetate. Sections were observed in a Tecnai T12 Spirit equipped with an Eagle 4kx4k camera (FEI Company), and large EM overviews were collected using the principles and software described by Ravelli and colleagues (79).

Disclosure of Potential Conflicts of Interest

Authors' Contributions

Acknowledgments

REFERENCES

1. Squier C, Kremer M. Biology of oral mucosa and esophagus. J Natl Cancer Inst Monogr 2001;29:7–15.
2. Fitzmaurice C, Allen C, Barber RM, Barregard L, Bhutta ZA, Brenner H, et al. Global, regional, and National cancer incidence, mortality, years of life lost, years lived with disability, and disability-adjusted life-years for 32 cancer groups, 1990 to 2015: a systematic analysis for the global burden of disease study. JAMA Oncol 2017;3:524–48.
3. Leemans CR, Snijders PJF, Brakenhoff RH. The molecular landscape of head and neck cancer. Nat Rev Cancer 2018;18:269–82.
4. Argiris A, Karamouzis M V, Raben D, Ferris RL. Head and neck cancer. Lancet 2008;371:1695–709.
5. Barretina J, Caponigro G, Stransky N, Venkatesan K, Margolin AA, Kim S, et al. The Cancer Cell line Encyclopedia enables predictive modelling of anticancer drug sensitivity. Nature 2012;483:603–7.
6. Smits JPH, Niehues H, Rikken G, Van Vlijmen-Willems I, Van De Zande G, Zeeuwen PLJM, et al. Immortalized N/TERT keratinocytes as an alternative cell source in 3D human epidermal models. Sci Rep 2017;7:11838.
7. Mery B, Rancoule C, Guy J-B, Espenel S, Wozny A-S, Battiston-Montagne P, et al. Preclinical models in HNSCC: a comprehensive review. Oral Oncol 2017;65:51–6.
8. Laban S, Steinmeister L, Gleißner L, Grob TJ, Grénman R, Petersen C, et al. Sorafenib sensitizes head and neck squamous cell carcinoma cells to ionizing radiation. Radiother Oncol 2013;109:286–92.
9. Maushagen R, Reers S, Pfannerstill AC, Hahlbrock A, Stauber R, Rahmanzadeh R, et al. Effects of paclitaxel on permanent head and neck squamous cell carcinoma cell lines and identification of anti-apoptotic caspase 9b. J Cancer Res Clin Oncol 2016;142:1261–71.
10. Voskoglou-Nomikos T, Pater JL, Seymour L. Clinical predictive value of the *in vitro* cell line, human xenograft, and mouse allograft preclinical cancer models. Clin Cancer Res 2003;9:4227–39.
11. Johnson JI, Decker S, Zaharevitz D, Rubinstein LV, Venditti JM, Schepartz S, et al. Relationships between drug activity in NCI preclinical *in vitro* and *in vivo* models and early clinical trials. Br J Cancer 2001;84:1424–31.
12. Kross KW, Heimdal JH, Olsnes C, Olofsson J, Aarstad HJ. Co-culture of head and neck squamous cell carcinoma spheroids with autologous monocytes predicts prognosis. Scand J Immunol 2008;67:392–9.

American Association for Cancer Research

13. Kohno N, Ohnuma T, Truog P. Effects of hyaluronidase on doxorubicin penetration into squamous carcinoma multicellular tumor spheroids and its cell lethality. J Cancer Res Clin Oncol 1994;120:293–7.

14. Braakhuis BJ, Sneeuwloper G, Snow GB. The potential of the nude mouse xenograft model for the study of head and neck cancer. Arch Otorhinolaryngol 1984;239:69–79.

15. Smith LP, Thomas GR.Animal models for the study of squamous cell carcinoma of the upper aerodigestive tract: a historical perspective with review of their utility and limitations. Part A. Chemically-induced de novo cancer, syngeneic animal models of HNSCC, animal models of transplanted xenogeneic human tumors. Int J Cancer 2006;118:2111–22.

16. Tanaka N, Osman AA, Takahashi Y, Lindemann A, Patel AA, Zhao M, et al. Head and neck cancer organoids established by modification of the CTOS method can be used to predict in vivo drug sensitivity. Oral Oncol 2018;87:49–57.

17. Neal JT, Li X, Zhu J, Giangarra V, Grzeskowiak CL, Ju J, et al. Organoid modeling of the tumor immune microenvironment. Cell 2018;175:1972–88.

18. Clarkson E, Mashkoor F, Abdulateef S. Oral viral infections: diagnosis and management. Dent Clin North Am 2017;61:351–63.

19. Sayers CL, Elliott G.Herpes Simplex Virus 1 enters human keratinocytes by a Nectin-1-dependent, rapid plasma membrane fusion pathway that functions at low temperature. J Virol 2016;90:10379–89.

20. D'Souza G, Kreimer AR, Viscidi R, Pawlita M, Fakhry C, Koch WM, et al. Case–control study of human papillomavirus and oropharyngeal cancer. N Engl J Med 2007;356:1944–56.

21. Griffin LM, Cicchini L, Xu T, Pyeon D. Human keratinocyte cultures in the investigation of early steps of human papillomavirus infection. Methods Mol Biol 2014;219–238.

22. Drost J, Clevers H.Organoids in cancer research. Nat Rev Cancer 2018; 18:407–18.

23. Vlachogiannis G, Hedayat S, Vatsiou A, Jamin Y, Fernández-Mateos J, Khan K, et al. Patient-derived organoids model treatment response of metastatic gastrointestinal cancers. Science 2018;926:920–6.

24. Etienne L, Joshi P, Dingle L, Huang E, Grzesik P, Desai PJ. Visualization of herpes simplex virus type 1 virions using fluorescent colors. J Virol Methods 2017;241:46–51.

25. Gillison ML, Lowy DR.A causal role for human papillomavirus in head and neck cancer. Lancet 2004;363:1488–9.

26. Pyeon D, Lambert PF, Ahlquist P. Production of infectious human papillomavirus independently of viral replication and epithelial cell differentiation. Proc Natl Acad Sci U S A 2005;102:9311–6.

27. Van De Wetering M, Francies HE, Francis JM, Bounova G, Iorio F, Pronk A, et al. Prospective derivation of a living organoid biobank of colorectal cancer patients. Cell 2015;161:933–45.

28. Fujii M, Shimokawa M, Date S, Takano A, Matano M, Nanki K, et al. A colorectal tumor organoid library demonstrates progressive loss of niche factor requirements during Tumorigenesis. Cell Stem Cell 2016;18:827–38.

29. Vassilev LT, Vu BT, Graves B, Carvajal D, Podlaski F, Filipovic Z, et al. In vivo activation of the p53 pathway by small-molecule antagonists of MDM2. Science 2004;303:844–8.

30. The Cancer Genome Atlas Network. Comprehensive genomic characterization of head and neck squamous cell carcinomas. Nature 2015;517:576–82.

31. Freed-Pastor WA, Prives C. Mutant p53: one name, many proteins. Genes Dev 2012;26:1268–86.

32. Love MI, Huber W, Anders S. Moderated estimation of fold change and dispersion for RNA-seq data with DESeq2. Genome Biol 2014;15:550.

33. Schrader CH, Kolb M, Zaoui K, Flechtenmacher C, Grabe N, Weber KJ, et al. Kallikrein-related peptidase 6 regulates epithelial-to-mesenchymal transition and serves as prognostic biomarker for head and neck squamous cell carcinoma patients. Mol Cancer 2015;14:107.

34. Zolk O, Schnepf R, Muschler M, Fromm MF, Wendler O, Traxdorf M, et al. Transporter gene expression in human head and neck squamous cell carcinoma and associated epigenetic regulatory mechanisms. Am J Pathol 2013;182:234–43.

35. Castillo-González AC, Nieto-Cerón S, Pelegrín-Hernández JP, Montenegro MF, Noguera JA, López-Moreno MF, et al. Dysregulated cholinergic network as a novel biomarker of poor prognostic in patients with head and neck squamous cell carcinoma. BMC Cancer 2015;15:385.

36. Bhosale PG, Cristea S, Ambatipudi S, Desai RS, Kumar R, Patil A, et al. Chromosomal alterations and gene expression changes associated with the progression of leukoplakia to advanced gingivobuccal cancer. Transl Oncol 2017;10:396–409.

37. Yan L, Zhan C, Wu J, Wang S. Expression profile analysis of head and neck squamous cell carcinomas using data from The Cancer Genome Atlas. Mol Med Rep 2016;13:4259–65.

38. Gonzalez HE, Gujrati M, Frederick M, Henderson Y, Arumugam J, Spring PW, et al. Identification of 9 genes differentially expressed in head and neck squamous cell carcinoma. Arch Otolaryngol Head Neck Surg 2003;129:754–9.

39. Stransky N, Egloff AM, Tward AD, Kostic AD, Cibulskis K, Sivachenko A, et al. The mutational landscape of head and neck squamous cell carcinoma. Science 2011;333:1157–60.

40. van Jaarsveld RH, Kops GJPL. Difference makers: chromosomal instability versus aneuploidy in cancer. Trends Cancer 2016;2:561–71.

41. Lengauer C, Kinzler KW, Vogelstein B. Genetic instability in colorectal cancers. Nature 1997;384:623–7.

42. Koo BK, Stange DE, Sato T, Karthaus W, Farin HF, Huch M, et al. Controlled gene expression in primary Lgr5 organoid cultures. Nat Methods 2012;9:81–3.

43. Cavalieri S, Perrone F, Miceli R, Ascierto PA, Locati LD, Bergamini C, et al. Efficacy and safety of single-agent pan-human epidermal growth factor receptor (HER) inhibitor dacomitinib in locally advanced unresectable or metastatic skin squamous cell cancer. Eur J Cancer 2018;97:7–15.

44. Soulières D, Faivre S, Mesía R, Remenár É, Li SH, Karpenko A, et al. Buparlisib and paclitaxel in patients with platinum-pretreated recurrent or metastatic squamous cell carcinoma of the head and neck (BERIL-1): a randomised, double-blind, placebo-controlled phase 2 trial. Lancet Oncol 2017;18:323–35.

45. Machiels JPH, Haddad RI, Fayette J, Licitra LF, Tahara M, Vermorken JB, et al. Afatinib versus methotrexate as second-line treatment in patients with recurrent or metastatic squamous-cell carcinoma of the head and neck progressing on or after platinum-based therapy (LUX-Head & Neck 1): An open-label, randomised phase 3 trial. Lancet Oncol 2015;16:583–94.

46. Machiels JP, Bossi P, Menis J, Lia M, Fortpied C, Liu Y, et al. Activity and safety of afatinib in a window preoperative EORTC study in patients with squamous cell carcinoma of the head and neck (SCCHN). Ann Oncol 2018;29:985–91.

47. Bossi P, Resteghini C, Paielli N, Licitra L, Pilotti S, Perrone F. Prognostic and predictive value of EGFR in head and neck squamous cell carcinoma. Oncotarget 2016;7:74362–79.

48. Andersson A, Fagerberg J, Lewensohn R, Ehrsson H. Pharmacokinetics of cisplatin and its monohydrated complex in humans. J Pharm Sci 1996;85:824–7.

49. Perez RP, O'Dwyer PJ, Handel LM, Ozols RF, Hamilton TC. Comparative cytotoxicity of CI-973, cisplatin, carboplatin and tetraplatin in human ovarian carcinoma cell lines. Int J Cancer 1991;48:265–9.

50. Atsushi H, Shuji S, Kosuke A, Takafumi K. A comparison of in vitro platinum-DNA adduct formation between carboplatin and cisplatin. Int J Biochem 1994;26:1009–16.

51. Guan J, Li Q, Zhang Y, Xiao N, Chen M, Zhang Y, et al. A meta-analysis comparing cisplatin-based to carboplatin-based chemotherapy in moderate to advanced squamous cell carcinoma of head and neck (SCCHN). Oncotarget 2016;7:7110–9.

52. Sun W, Yan H, Qian C, Wang C, Zhao M, Liu Y, et al. Cofilin-1 and phosphoglycerate kinase 1 as promising indicators for glioma radiosensibility and prognosis. Oncotarget 2017;8:55073–83.

53. Pelosof L, Yerram S, Armstrong T, Chu N, Danilova L, Yanagisawa B, et al. GPX3 promoter methylation predicts platinum sensitivity in colorectal cancer. Epigenetics 2016;12:540–50.

54. Lenarduzzi M, Hui ABY, Alajez NM, Shi W, Williams J, Yue S, et al. MicroRNA-193b enhances tumor progression via down regulation of neurofibromin 1. PLoS One 2013;8:e53765.

55. Castle JC, Loewer M, Boegel S, de Graaf J, Bender C, Tadmor AD, et al. Immunomic, genomic and transcriptomic characterization of CT26 colorectal carcinoma. BMC Genomics 2014;15:190.

56. Fulda S, Vucic D. Targeting IAP proteins for therapeutic intervention in cancer. Nat Rev Drug Discov 2012;11:331.

57. Eytan DF, Snow GE, Carlson S, Derakhshan A, Saleh A, Schiltz S, et al. SMAC mimetic birinapant plus radiation eradicates human head and neck cancers with genomic amplifications of cell death genes FADD and BIRC2. Cancer Res 2016;76:5442–54.

58. Hanahan D, Weinberg RA. Hallmarks of cancer: The next generation. Cell 2011;144:646–74.

59. Seiwert TY, Salama JK, Vokes EE. The chemoradiation paradigm in head and neck cancer. Nature Clinical Practice Oncology 2007;4:156–71.

60. Fritsch C, Huang A, Chatenay-Rivauday C, Schnell C, Reddy A, Liu M, et al. Characterization of the novel and specific PI3K inhibitor NVP-BYL719 and development of the patient stratification strategy for clinical trials. Mol Cancer Ther 2014;13:1117–29.

61. Juric D, Rodon J, Tabernero J, Janku F, Burris HA, Schellens JHM, et al. Phosphatidylinositol 3-Kinase α–selective inhibition with alpelisib (BYL719) in PIK3CA-altered solid tumors: results from the first-in-human study. J Clin Oncol 2018;36:1291–9.

62. Mayer IA, Abramson VG, Formisano L, Balko JM, Estrada M V, Sanders ME, et al. A phase Ib study of alpelisib (BYL719), a PI3Kα-specific inhibitor, with letrozole in ER+/HER2-negative metastatic breast cancer. Clin Cancer Res 2017;23:26–34.

63. Gild ML, Landa I, Ryder M, Ghossein RA, Knauf JA, Fagin JA. Targeting mTOR in RET mutant medullary and differentiated thyroid cancer cells. Endocr Relat Cancer 2013;20:659–67.

64. Gavine PR, Mooney L, Kilgour E, Thomas AP, Al-Kadhimi K, Beck S, et al. AZD4547: An orally bioavailable, potent, and selective inhibitor of the fibroblast growth factor receptor tyrosine kinase family. Cancer Res 2012;72:2045–56.

65. Zhu X, Ding X. Study on a 3D Hydrogel-Based culture model for characterizing growth of fibroblasts under viral infection and drug treatment. SLAS Discov 2017;22:626–34.

66. Valyi-Nagy T, Fredericks B, Ravindra A, Hopkins J, Shukla D, Valyi-Nagy K. Herpes simplex virus type 1 infection promotes the growth of a subpopulation of tumor cells in 3D uveal melanoma cultures. J Virol 2018;92:e00700–18.

67. Bonner J a, Harari PM, Giralt J, Azarnia N, Shin DM, Cohen RB, et al. Radiotherapy plus cetuximab for squamous-cell carcinoma of the head and neck. N Engl J Med 2006;354:567–78.

68. Cai Y, Dodhia S, Su GH. Dysregulations in the PI3K pathway and targeted therapies for head and neck squamous cell carcinoma. Oncotarget 2017;8:22203–17.

69. Munster P, Elkabets M, Gilbert J, Razak ARA, Ahn M-J, Yen C-J, et al. Abstract A46: Inhibition of PIK3CA with BYL719 can overcome resistance to cetuximab in squamous cell carcinoma of the head and neck (SCCHN). Mol Cancer Ther 2015;14:A46.

70. Ho A, Chau N, Brana Garcia I, Ferte C, Even C, Burrows F, et al. Preliminary results from a phase 2 trial of tipifarnib in HRAS-mutant head and neck squamous cell carcinomas. Int J Radiat Oncol Biol Phys 2018;100:1367.

71. Economopoulou P, Perisanidis C, Giotakis EI, Psyrri A. The emerging role of immunotherapy in head and neck squamous cell carcinoma (HNSCC): anti-tumor immunity and clinical applications. Ann Transl Med 2016;4:173–173.

72. Dijkstra KK, Cattaneo CM, Weeber F, Chalabi M, van de Haar J, Fanchi LF, et al. Generation of tumor-reactive T cells by co-culture of peripheral blood lymphocytes and tumor organoids. Cell 2018;174:1586–98.

73. Hashimshony T, Wagner F, Sher N, Yanai I. CEL-Seq: single-cell RNA-seq by multiplexed linear amplification. Cell Rep 2012;2:666–73.

74. Simmini S, Bialecka M, Huch M, Kester L, van de Wetering M, Sato T, et al. Transformation of intestinal stem cells into gastric stem cells on loss of transcription factor Cdx2. Nat Commun 2014;5:5728.

75. Li H, Durbin R. Fast and accurate long-read alignment with Burrows-Wheeler transform. Bioinformatics 2010;26:589–95.

76. Hoogstraat M, Hinrichs JWJ, Besselink NJM, Radersma-Van Loon JH, De Voijs CMA, Peeters T, et al. Simultaneous detection of clinically relevant mutations and amplifications for routine cancer pathology. J Mol Diagnostics 2015;7:10–8.

77. Shaner NC, Lambert GG, Chammas A, Ni Y, Cranfill PJ, Baird MA, et al. A bright monomeric green fluorescent protein derived from Branchiostoma lanceolatum. Nat Methods 2013;10:407–9.

78. Huch M, Dorrell C, Boj SF, van Es JH, Li VSW, van de Wetering M, et al. In vitro expansion of single Lgr5+ liver stem cells induced by Wnt-driven regeneration. Nature 2013;494:247–50.

79. Faas FGA, Avramut MC, van den Berg BM, Mommaas AM, Koster AJ, Ravelli RBG. Virtual nanoscopy: generation of ultra-large high resolution electron microscopy maps. J Cell Biol 2012;198:457–69.